Science of the Total Environment 989 (2025) 179881

Contents lists available at ScienceDirect

Science of the Total Environment

journal homepage: www.elsevier.com/locate/scitotenv

Aging and climate change-induced heat stress synergistically increase susceptibility to *Vibrio vulnificus* infection via an altered gut microbiome-immune axis

Subhajit Roy [a], Madhura More [a], Ayushi Trivedi [a], Punnag Saha [a,f], Dipro Bose [a], Susmita Das [b], Zahid Hayat Mahmud [b], S.M. Manzoor Ahmed Hanifi [c], Saurabh Chatterjee [a,d,e,*]

[a] Environmental Health and Disease Laboratory, Department of Environmental and Occupational Health, Program in Public Health, Susan and Henry Samueli College of Health Sciences, University of California, Irvine, CA 92697, USA
[b] Health Systems and Population Studies Division, International Centre for Diarrhoeal Disease Research, Bangladesh (icddr, b), Dhaka 1212, Bangladesh
[c] Laboratory of Environmental Health, International Centre for Diarrhoeal Disease Research, Bangladesh (icddr, b), Dhaka 1212, Bangladesh
[d] Division of Infectious Diseases, School of Medicine, University of California, Irvine, CA 92697, USA
[e] Long Beach VA Medical Center, Long Beach, CA 90288, USA
[f] Department of Pediatrics, University of California San Diego, La Jolla, CA 92093, USA

HIGHLIGHTS

- Aging and heat stress together increase *Vibrio vulnificus* infection severity in mice.
- Periodic heat exposure impairs gut barrier and accelerates T-cell immunosenescence.
- Aged mice show heightened systemic inflammation and endotoxemia under dual stress.
- Heat stress disrupts microbial diversity and enriches antibiotic resistance genes.
- Recolonization with key probiotics restored intestinal health and immune regulation.

GRAPHICAL ABSTRACT

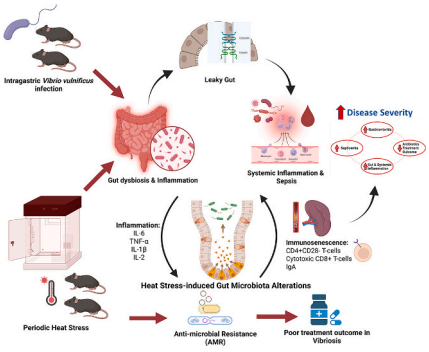

ARTICLE INFO

Editor: Daqiang Yin

Keywords:
Global warming
Environmental heat load
Vibriosis
Human health
Host-microbiota-immune interaction
Antibiotic resistance genes

ABSTRACT

Climate change is exacerbating heatwaves, significantly increasing public health risks, including heightened vulnerability to *Vibrio vulnificus* infections, especially among older adults. While heat stress alone impairs immune regulation and compromises gut integrity, the combined effects of aging and climate-induced heat stress on infectious severity remain insufficiently explored. Using young (12-week-old) and aged (24-month-old) mouse models, we examined how aging and periodic heat stress synergistically influence susceptibility to *Vibrio vulnificus* by assessing gut microbiome alterations, immune responses, and antibiotic resistance gene dynamics. Heat stress markedly impaired intestinal barrier function, induced significant microbiome shifts, elevated systemic inflammation, and promoted enrichment of antibiotic resistance genes particularly those conferring tetracycline

* Corresponding author at: Environmental Health and Disease Laboratory, Department of Environmental and Occupational Health, Program in Public Health, Susan and Henry Samueli College of Health Sciences, University of California, Irvine, CA 92697, USA.
E-mail address: saurabhc@hs.uci.edu (S. Chatterjee).

https://doi.org/10.1016/j.scitotenv.2025.179881
Received 17 May 2025; Received in revised form 3 June 2025; Accepted 8 June 2025
Available online 13 June 2025

Resistome
T-cell immunosenescence

resistance with effects significantly amplified in aged mice. Upon *Vibrio vulnificus* infection, aged heat-stressed mice demonstrated elevated inflammatory responses, severe intestinal damage, and pronounced immune dysregulation compared to younger counterparts. Gut depletion and probiotic recolonization models further validated microbiota involvement, showing that *Roseburia intestinalis* significantly reduced heat stress-exacerbated $CD4^+$ T-cell immunosenescence in aged mice. Collectively, this study provides robust experimental evidence highlighting the critical interplay between aging and climate-driven heat stress in intensifying infectious disease severity via microbiome–immune axis disruptions, underscoring the need for microbiota-targeted strategies in climate-vulnerable populations.

1. Introduction

Heat stress, a condition marked by the body's struggle to regulate its temperature, engendered profound physiological disruptions and, in severe instances, culminated in fatalities (Ebi et al., 2021a). This risk was exacerbated during periods of elevated temperatures and heatwaves, which correlated with a significant uptick in mortality rates, particularly among the elderly (*MMWR Morb. Mortal. Wkly. Rep.*, 2022). Climate change exacerbates global heat waves, significantly impacting public health, ecosystems, and infrastructure (Marx et al., 2021), (Ebi et al., 2021b). Human activities have worsened these prolonged hot weather events, as evidenced by the 2021 Pacific Northwest heat dome surpassing 115 °F (Ballester et al., 2023), (Perkins-Kirkpatrick and Lewis, 2020). In the U.S., heat wave frequency and duration have increased markedly from 1949 to 2005 (Grundstein and Dowd, 2011), aligning with findings of significant rises in heatwave occurrence and intensity since the 1950s. Since 1979, heatwaves have been 67 % more frequent and 20 % longer, extending from 8 to 12 days, and are moving 20 % more slowly due to weakening jet streams (Luo et al., 2024). Studies indicate recent heat waves, such as the 2022 European and 2023 China events, would be nearly unimaginable without anthropogenic climate change (Marx et al., 2021). Models link the worsening heat waves over the past 45 years to greenhouse gas emissions, significantly increasing cumulative heat (Marx et al., 2021). Nationwide projections in the United States portended an alarming trend, foreseeing a surge in heat-related deaths by over 90 %. The situation was especially dire on the west coast of the United States, where projections hinted at a sevenfold increase in heat-related fatalities in the forthcoming decades (Knowlton et al., 2007), (Hayhoe et al., 2004). Effective management and adaptation strategies are essential for mitigating these impacts and improving outcomes for vulnerable populations.

Extensive mechanistic work has clarified how elevated core temperature translates into organ injury. Heat exposure accelerates mitochondrial respiration, elevates reactive oxygen species, and triggers a heat-shock response that intersects with NF-κB (Nuclear factor-κB) and MAPK (mitogen-activated protein kinase) pathways, amplifying transcription of pro-inflammatory cytokines (McMichael and Lindgren, 2011). These signals converge on the intestinal epithelium: tight-junction proteins claudin-1, occludin, and ZO-1 (Zonula Occludens-1) are depleted, epithelial permeability increases, and bacterial lipopolysaccharide leaks into the circulation (Sharma et al., 1992), (Lee et al., 2015). The resulting endotoxemia elevates systemic IL-6, TNF-α, and IL-1β and skews T-cell polarization toward a pro-inflammatory phenotype (Wen et al., 2021a). Research conducted in our laboratory and by other groups has elucidated the immunomodulatory effects of heat stress in both systemic and organ-specific contexts (Roy et al., 2024), (Hammami et al., 1998). Furthermore, heat stress has been shown to significantly alter T-cell responses in avian models (Hirakawa et al., 2020) and compromise gut barrier integrity, with distinct gut immune responses observed in bovine models (Koch et al., 2019). Intestinal microbiota was a crucial mediator of intestinal immunity and gut barrier integrity (Kamada et al., 2013), (Zheng et al., 2020), (Paone and Cani, 2020). Heat stress was well-documented for its role in inducing gut dysbiosis and conclusively shown to cause significant intestinal inflammation (Xia et al., 2022), (Hu et al., 2022). Previously, heat stress has also been reported to compromise the immune response against bacterial pathogens in non-mammalian systems (Yang et al., 2022). However, most mechanistic evidence derives from young or otherwise healthy models, leaving age-specific effects on the gut-microbiome–immune axis poorly defined. Accordingly, we aimed to create a murine periodic heat-wave model with 40 °C at 60 % relative humidity for 3 h each day over 14 days to mirror the recurrent thermal events that endanger older adults and to test whether sustained heat stress disrupts the gut microbiome–immune axis and heightens susceptibility to infections (Trinanes and Martinez-Urtaza, 2021).

Globally, *Vibrio* infections are increasing, with projections indicating a significant rise in coastal areas suitable for *Vibrio* by 2100 under adverse climate scenarios (Bastin et al., 2024). The number of people living in such zones has almost doubled since 1980, and warmer seas are now pushing *Vibrio* habitats into higher-latitude parts of Europe and Asia (Bastin et al., 2024), (Hegde et al., 2024). Regional surveillance illustrates the trend. Bangladesh records >100,000 *Vibrio cholerae* cases each year (Islam et al., 2023). Data collected from 2000 to 2021 show widespread urban and rural impact, frequent co-infections (Parvin et al., 2021), (Shishir et al., 2018), (Das et al., 2023) and increased antibiotic resistance to the pathogen (Fleischmann et al., 2022). Zambia lacks detailed incidence data, yet repeated cholera outbreaks linked to poor water, sanitation, and hygiene underline its vulnerability (Bastin et al., 2024). In the Baltic Sea region, summer heatwaves have brought more Vibrio infections related to seawater or seafood exposure as sea-surface temperatures rise (Amato et al., 2022). Three species dominate there: *V. alginolyticus*, *V. parahaemolyticus*, and *V. vulnificus* (Amato et al., 2022), (Riedinger et al., 2024), (Li et al., 2014). Similar patterns appear in other parts of the world. Along China's southern coast, *V. parahaemolyticus* has overtaken *Salmonella* as the leading bacterial cause of diarrhea, its range expanding with warmer coastal waters (Sheahan et al., 2022). In the United States, non-cholera Vibrio infections have climbed steadily for two decades, with *V. vulnificus* now the second most common species (Centers for Disease Control and Prevention (CDC), 2019). The CDC's COVIS program reports about 3000 Vibrio cases each year; >20 % come from *V. vulnificus*, mainly in Gulf Coast states but increasingly along the Atlantic and Pacific coasts, and the species carries high fatality rates (Zaidenstein et al., 2008), (Horseman and Surani, 2011), (Archer et al., 2023). Reports of *V. vulnificus* have risen eight-fold in the past 20 years, posing an especially high risk to older adults (Logar-Henderson et al., 2019), (Hughes et al., 2024). Cases cluster during hot summers that coincide with heatwaves, rising sea levels, and above-average coastal water temperatures (Morgado et al., 2024), (Logar-Henderson et al., 2019). Longitudinal surveillance on the United States east coast now shows emerging antibiotic resistance in this pathogen (Saha et al., 2022), consistent with broader evidence that climate change can accelerate antimicrobial resistance (Roy et al., 2023), (Zanobetti et al., 2012). Despite these clear epidemiological signals, three key gaps hinder effective risk assessment and intervention. First, we do not yet know how chronic heat exposure alters microbiome composition, antibiotic-resistance genes, and barrier integrity in aging hosts. Second, causal links among dysbiosis, epithelial damage, systemic inflammation, and immune changes have rarely been measured within a single experimental model. Third, no study has tested whether heat-induced gut microbiota alterations heighten susceptibility

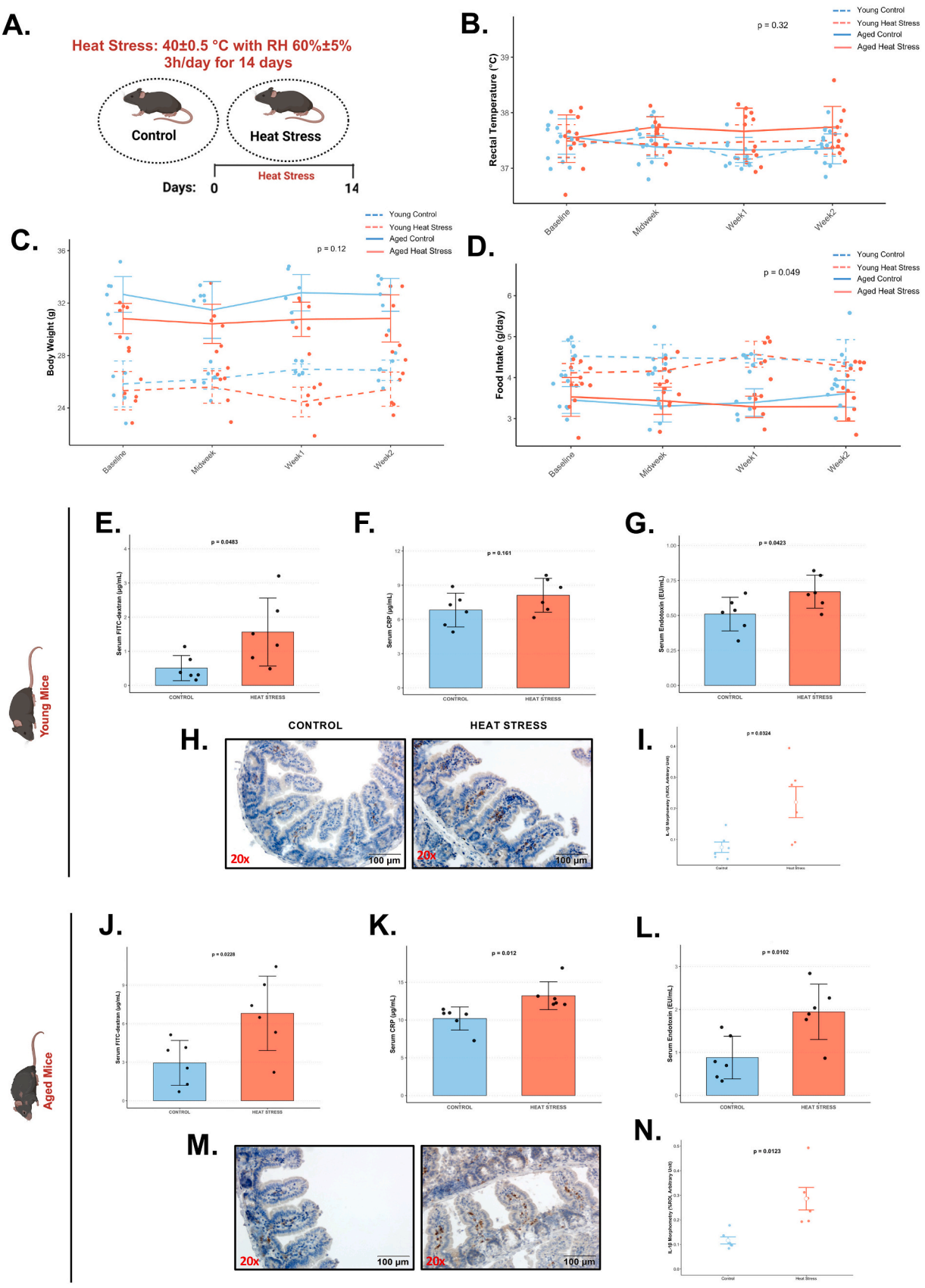

(caption on next page)

Fig. 1. Establishment of a periodic heat stress-induced mouse model and age-related differences in physiological and immunopathological markers. A. Schematic representation of the experimental design. B. Rectal temperature: recorded at baseline, midweek, Week 1, and Week 2. Statistical analysis was performed using a linear mixed-effects model (LME) with ANOVA for fixed effects and Tukey's test for pairwise comparisons ($p < 0.05$). C. Body weight: measured at the same time points. Analysis was conducted using an LME with ANOVA for fixed effects and Tukey's post hoc test ($p < 0.05$). D. Food intake: assessed at baseline, midweek, Week 1, and Week 2 using an LME, ANOVA for fixed effects, and Tukey's test ($p < 0.05$). Data for B, C, and D are presented as individual points with group means and SD error bars. Solid lines represent aged mice, while dashed lines represent young adult mice. Sky-blue and tomato colors denote control and heat stress groups, respectively. E. Serum FITC-dextran levels: intestinal permeability was measured in 12-week-old young adult mice. Levels (μg/mL) were displayed as bar plots with individual data points ($n = 6$ biological replicates, averaged from three technical replicates). Statistical analysis was conducted using an unpaired, two-tailed *t*-test with Benjamini-Hochberg correction ($p < 0.05$). F. Serum C-reactive protein (CRP): measured as a marker of systemic inflammation in 12-week-old young adult mice. Levels (μg/mL) were displayed as bar plots with individual data points ($n = 6$ biological replicates, averaged from three technical replicates). Statistical analysis was conducted using an unpaired, two-tailed t-test with Benjamini-Hochberg correction ($p < 0.05$). G. Serum endotoxin levels: serum endotoxin levels (EU/mL) were quantified in 12-week-old young adult mice to evaluate endotoxemia. Data were presented as bar plots with individual points ($n = 6$ biological replicates, averaged from three technical replicates). Statistical analysis was conducted using an unpaired, two-tailed *t*-test with Benjamini-Hochberg correction ($p < 0.05$). H. IL-1β immunohistochemistry: intestinal IL-1β expression was assessed in 12-week-old young adult mice using immunohistochemistry at 20× magnification (scale bar = 100 μm). I. Quantification of IL-1β immunoreactivity was expressed as arbitrary units and plotted on the ordinate. Data represent individual points with error bars for group means and SD, derived from 12 distinct microscopic fields per group ($n = 6$ biological replicates). Statistical analysis was conducted using an unpaired, two-tailed t-test with Benjamini-Hochberg correction ($p < 0.05$). J. Serum FITC-dextran levels: intestinal permeability was assessed in 24-week-old aged mice. Levels (μg/mL) were presented as bar plots with individual data points ($n = 6$ biological replicates, averaged from three technical replicates). Statistical analysis was performed using an unpaired, two-tailed t-test with Benjamini-Hochberg correction ($p < 0.05$). K. Serum C-reactive protein (CRP): measured as a marker of systemic inflammation in 24-week-old aged mice. Levels (μg/mL) were displayed as bar plots with individual data points ($n = 6$ biological replicates, averaged from three technical replicates). Statistical analysis was conducted using an unpaired, two-tailed t-test with Benjamini-Hochberg correction ($p < 0.05$). L. Serum endotoxin levels: serum endotoxin levels (EU/mL) were quantified in 24-week-old aged mice. Data were presented as bar plots with individual points ($n = 6$ biological replicates, averaged from three technical replicates). Statistical analysis was conducted using an unpaired, two-tailed t-test with Benjamini-Hochberg correction ($p < 0.05$). Data for J, K, and L are presented as individual points with group means and SD error bars. Sky-blue and tomato colors denote control and heat stress groups, respectively. M. IL-1β Immunohistochemistry: Intestinal IL-1β expression was assessed in 24-week-old aged mice using immunohistochemistry at 20× magnification (scale bar = 100 μm). N. Quantification of IL-1β immunoreactivity was expressed as arbitrary units and plotted on the ordinate. Data represent individual points with error bars for group means and SD, derived from 12 distinct microscopic fields per group ($n = 6$ biological replicates). Statistical analysis was conducted using an unpaired, two-tailed t-test with Benjamini-Hochberg correction ($p < 0.05$). All *p*-values in panels E through N were calculated with the significance threshold set at $p < 0.05$.

to *V. vulnificus*, a pathogen whose incidence is rising with coastal warming.

The present work addresses these gaps using aged mice exposed to sustained moderate hyperthermia that mirrors projected mid-century heat waves. The study combines whole metagenomic sequencing (WMS) to characterize microbial composition and antibiotic-resistance genes; quantifies barrier integrity through fluorescein isothiocyanate dextran permeability, serum lipopolysaccharide, and tight-junction protein abundance; profiles mucosal and systemic cytokines together with T-cell polarization; and evaluates host susceptibility after *Vibrio vulnificus* challenge. Integrating these established indicators with comprehensive microbiome data provides new insight into how a climate-relevant thermal stressor remodels the gut-immune axis in older hosts and clarifies its functional consequences for an emerging coastal pathogen.

2. Materials and methods

2.1. Animal model and study design

Twenty-three-month-old (Aged adult) and 12 weeks (Young adult) male C57BL/6J wild-type (WT) mice were purchased from Jackson Laboratories (Bar Harbor, ME, USA). These mice, free of pathogens, were selected due to their advanced age to study the physiological and microbiome changes associated with heat stress. Upon arrival, the mice were acclimated to the laboratory environment for a week to reduce transport-related stress and allow adaptation to their new surroundings. During this period, mice were housed in individually ventilated cages under controlled conditions, including a 12-hour light/dark cycle, stable ambient temperature (22 ± 2 °C), and humidity (40–60 %). Mice were provided with ad-libitum access to food and water throughout the study.

2.2. Heat stress exposure

Following a 7-day acclimation period, aged C57BL/6 J male mice ($n = 6$/group) were exposed to daily heat stress at 40 ± 0.5 °C and 60 ± 5 % relative humidity for 3 h over 14 consecutive days, using a controlled environmental chamber (Model RIS26SD, Powers Scientific Inc., Doylestown, PA, USA) (Trinanes and Martinez-Urtaza, 2021). This protocol extended prior heat stress paradigms by employing higher temperature and prolonged daily exposure to better mimic extreme heat events (Wen et al., 2021b), (Qu et al., 2021). Mice were monitored daily for clinical signs, including lethargy and weight loss, with no adverse effects noted. Mice were monitored daily for clinical signs, including lethargy and weight loss, with no adverse effects noted. Group sizes were determined by statistical power analysis to ensure adequate sensitivity for biological outcomes (Festing and Altman, 2002). To minimize cage-associated microbiome biases, animals were randomized by body weight into three cages per group, using a stratified method (Lipinski et al., 2021), (Witjes et al., 2020). Bi-weekly within-group cage rotation and tail markings ensured consistent tracking. Body weight and food intake were recorded at baseline (Day 0), midweek (~Day 3–4), Week 1, and Day 14. Food consumption was calculated per cage by subtracting uneaten food from the total provided; individual intake was estimated by dividing by mouse number and days per interval (Ali and Kravitz, 2018). Introducing a midweek measurement improved the resolution for detecting weight and food intake trends while avoiding excessive stress from handling (Qu et al., 2021). Body weight and food intake were monitored at baseline, mid-week, week 1, and again at the end of the 14-day heat-stress exposure; the full time-course results were plotted in Fig. 1B and C. At study completion, mice were euthanized under isoflurane anesthesia following NIH animal welfare guidelines, with approval from the University of California, Irvine IACUC (Protocol #AUP-22-132, approved February 21, 2023). Fecal samples were collected immediately before euthanasia, snap-frozen, and stored at −80 °C for microbiome analysis (Ericsson and Franklin, 2021), (DeBruyn and Hauther, 2017). Blood was collected via cardiac puncture for serum isolation, and tissues from the small intestine, colon, and liver were fixed in 10 % neutral buffered formalin for histological evaluation.

2.3. Measurements of rectal temperature

Rectal temperatures were measured using the BIOSEB TK8851 electronic thermometer (Braintree Scientific, Pinellas Park, FL, USA)

with a compatible rodent probe. The device provided accurate and consistent physiological readings, with measurements taken by gently inserting the probe into the rectum of each mouse. This method ensured reliable monitoring during experimental procedures.

2.4. Intragastric Vibrio vulnificus infection

The *Vibrio vulnificus* strain (ATCC 27562; strain designation 324 [CDC B9629]) was obtained from the American Type Culture Collection (Manassas, VA, USA). Bacteria were cultured in Luria-Bertani (LB) broth supplemented with 0.85 % sodium chloride (NaCl) (LB-N) or on LB-N agar plates with 1.5 % agar (Fisher Scientific, Waltham, MA, USA), providing optimal saline conditions for *V. vulnificus* growth. For infection, an overnight starter culture was grown statically at 30 °C in LB-N broth, then diluted 1:10 in pre-warmed LB-N and incubated with shaking at 30 °C until reaching exponential phase ($OD_{420} \approx 0.8$). Cultures were centrifuged at 13,800 ×*g* for 10 min, washed, and resuspended in sterile 1× phosphate-buffered saline (PBS; Thermo Fisher Scientific, Grand Island, NY, USA). Mice were intragastrically inoculated with 10^8 CFU/100 μL *V. vulnificus* via oral gavage. Control groups received 100 μL sterile PBS. Infections were performed once, with experimental endpoints set at 24 h post-inoculation. This protocol follows established models for *V. vulnificus* infection, offering a reproducible system to study host-pathogen dynamics and gastrointestinal disease mechanisms (Starks et al., 2000), (Gavin and Satchell, 2017).

2.5. Antibiotic-mediated gut depletion

Antibiotic-treated groups received an oral gavage of a broad-spectrum cocktail comprising metronidazole, neomycin, vancomycin, and ampicillin at 1 g/kg body weight, with an additional 0.5 g/kg of ampicillin, all sourced from Sigma-Aldrich (St. Louis, MO, USA), dissolved in sterile phosphate-buffered saline (PBS). The treatment was administered daily for 14 consecutive days. This regimen was based on previously validated protocols, including whole metagenome sequencing (WMS)-confirmed depletion from our prior studies (Bose et al., 2024), with minor modifications adopted from earlier published models (Daharsh et al., 2019), (Tirelle et al., 2020).

2.6. Post-antibiotic gut recolonization and heat stress challenge

Following microbiota depletion, twenty-three-month-old male C57BL/6J wild-type (WT) mice were recolonized with *Bifidobacterium pseudolongum*, *Akkermansia muciniphila*, and *Roseburia intestinalis*. Lyophilized strains were obtained from Creative Biolabs (Shirley, NY, USA): *B. pseudolongum* (Cat# LBGF-0324-GF4), *A. muciniphila* (Cat# LBST-010FG), and *R. intestinalis* (Cat# LBSX-0522-GF42). Bacterial cultures were grown anaerobically in optimized media. *Bifidobacterium pseudolongum* was cultured in MRS broth supplemented with 0.05 % cysteine hydrochloride and 20 g/L glucose at 37 °C (OD_{600}: 0.6–0.8; 10–12 h). *Akkermansia muciniphila* was grown in BHI broth containing 0.5 % porcine gastric mucin, 10 g/L glucose, and 2 g/L yeast extract at 37 °C (OD_{600}: 0.4–0.6; 24–48 h). *Roseburia intestinalis* was cultured in YCFA medium with 0.5 g/L acetate, 0.2 g/L butyrate, and 15 g/L glucose at 37 °C (OD_{600}: 0.8–1.0; 12–16 h). Cells were harvested, washed in sterile PBS, and resuspended in cryoprotective buffer (10 % skim milk powder, 5 % trehalose), then frozen at −80 °C and lyophilized. Powders were stored at −20 °C and subjected to CFU and viability checks. Prior to use, lyophilized preparations were reconstituted in sterile 1× PBS to administer *B. pseudolongum* (10^9 CFU), *A. muciniphila* (10^8 CFU), and *R. intestinalis* (10^8 CFU) via oral gavage daily for four days, following established protocols for effective gut colonization (Song et al., 2023), (Hänninen et al., 2018), (Kang et al., 2023), (Shen et al., 2022).

2.7. Microbiome and resistome analysis workflow

To investigate the gut microbiome's role in age-related exacerbation of *Vibrio vulnificus* immunopathology, twenty-three-month-old (aged adult) male C57BL/6J wild-type (WT) mice ($n = 5$/group) were used to compare Control and Heat Stress groups. A temporal microbiome analysis was also conducted in the Heat Stress group (n = 5/timepoint) at baseline (Day 0), Day 7, and Day 14. Microbiome and resistome workflows included DNA extraction, library preparation, sequencing, and bioinformatic analysis. For DNA extraction, 250 μL of liquid or 250 mg of solid fecal sample was processed using the PowerBead Pro Kit (QIAGEN, Cat# 47014; Germantown, MD, USA). Samples were homogenized with buffer CD1, centrifuged, and supernatants processed with buffers CD2 and CD3. Lysates were passed through a filter plate and washed with buffers EA and C5. After drying, DNA was eluted with buffer C6 and quantified using the Qubit High Sensitivity dsDNA Assay Kit (Thermo Fisher Scientific, Cat# Q32851; Waltham, MA, USA) on a Qubit 4 Fluorometer. Library preparation was performed using the Nextera XT DNA Library Prep Kit (Illumina, Cat# FC-131-1096; San Diego, CA, USA). Genomic DNA was tagmented, indexed, and amplified via thermal cycling. Purification was done using AMPure XP magnetic beads (Beckman Coulter, Cat# A63881; Indianapolis, IN, USA). Final libraries were eluted in EB buffer, quantified again, and pooled in equimolar concentrations. Sequencing was conducted on the NovaSeq S4 platform (Illumina; San Diego, CA, USA) using 2 × 150 bp paired-end reads, targeting 20 million reads per sample. ZymoBIOMICS Microbial Community Standard (Zymo Research, Cat# D6300; Irvine, CA, USA) served as the positive control, and extraction and library blanks were used as negative controls.

Bioinformatics was performed using the CosmosID-HUB platform (CosmosID Inc.; Rockville, MD, USA), aligning reads to curated microbial genome, virulence, and AMR databases. Resistome profiles were normalized as reads per kilobase per million mapped reads (RPKM), and filtering minimized false positives. Functional annotations were verified against known resistance mechanisms. Microbial and resistome diversity metrics were calculated using scikit-bio (Anaconda, Python-based; Austin, TX, USA). Alpha (Chao1, Shannon, Simpson) and beta diversity (Bray-Curtis, UniFrac) were assessed using PERMANOVA. Network analysis of microbial taxa, cytokines, and gut barrier integrity was performed using igraph and ggraph packages (R Foundation; Vienna, Austria). Nodes represented key taxa (*Roseburia intestinalis*, *Bifidobacterium pseudolongum*, *Akkermansia muciniphila*), cytokines (IL-2, IL-6, IL-1β, TNF-α), $CD4^+CD28^-$ and $CD8^+$ T cells, SCFA production, and barrier markers. Edges reflected literature-derived weights from KEGG, MicrobiomeDB, and PubMed. A second network linked virulence genes (e.g., *tetQ*, *bmhA*, *IS942*) to *Bacteroides* species (*B. fragilis*, *B. caecimuris*) under heat stress.

Access to the entire sequencing data is available via the Sequence Read Archive (SRA) database, accession ID: PRJNA1106799, accessible at https://www.ncbi.nlm.nih.gov/sra/PRJNA1106799.

2.8. FITC-dextran assay for intestinal permeability

Intestinal permeability was assessed using a standardized FITC-dextran assay. Mice were fasted for 4 h, with water withheld during the final 2 h. FITC-dextran (4 kDa; Sigma-Aldrich, Cat# FD4, St. Louis, MO, USA) was dissolved in sterile 1× PBS at 80 mg/mL, vortexed, and filtered through a 0.22-μm sterile membrane. Mice received 600 mg/kg body weight of FITC-dextran via oral gavage. Four hours post-gavage, blood was collected via cardiac puncture under isoflurane anesthesia. Serum was obtained after centrifugation of clotted blood at 4000 ×g for 10 min at 4 °C. Fluorescence was measured at 485 nm excitation and 535 nm emission using a microplate reader. FITC-dextran concentrations were calculated against a standard curve and expressed in μg/mL. All samples were run in triplicate for accuracy.

2.9. Immunohistochemistry

Intestinal sections were deparaffinized and subjected to epitope retrieval using solution (Cat# NC0196883) and a steamer from IHC-World (Woodstock, MD, USA). Endogenous peroxidase activity was quenched with 3 % hydrogen peroxide (Cat# H324-500; Fisher Scientific, Waltham, MA, USA) for 20 min. Blocking was performed with 5 % goat serum (Cat# 16210064; Thermo Fisher Scientific, Grand Island, NY, USA) for 1 h. Primary antibodies against IL-1β (Cat# sc-52012) and IL-2 (Cat# sc-133118CD28) from Santa Cruz Biotechnology (Dallas, TX, USA), and CD28 (Cat# ab243228) from Abcam Limited (Waltham, MA, USA) were diluted in blocking buffer and incubated overnight at 4 °C. Species-specific biotinylated secondary antibodies (Cat# BA-9200, BA-1000) and the Vectastain Elite ABC Kit (Cat# PK-6100) were procured from Vector Laboratories (Burlingame, CA, USA). DAB substrate (Cat# D5905) and Mayer's hematoxylin (Cat# MHS80) from Sigma-Aldrich (St. Louis, MO, USA) were used for signal detection and counterstaining. Washing was carried out with PBS-T (PBS + 0.05 % Tween 20) between steps. Sections were mounted using Lerner Aqua Mount (Cat# 41799-008; Thermo Fisher Scientific, Grand Island, NY, USA). Imaging and morphometric analyses were conducted using an Olympus BX63 microscope and cellSens Software V2.2 (Olympus, Center Valley, PA, USA).

2.10. Immunofluorescence

Formalin-fixed, paraffin-embedded intestinal sections were deparaffinized and subjected to epitope retrieval using IHC World's retrieval solution and steamer (Ellicott City, MD, USA), following the manufacturer's protocol. Primary antibodies against Hsp70 (Cat# ab2787) and Occludin (Cat# ab216327) were sourced from Abcam Limited (Waltham, MA, USA) and applied at recommended dilutions, with overnight incubation at 4 °C. For unconjugated primaries, Alexa Fluor 633-conjugated (Cat# A21082) or 488-conjugated (Cat# A11055) secondary antibodies were used (Invitrogen, Waltham, MA, USA). Sections were mounted using ProLong Gold antifade mounting media with DAPI (4′,6-diamidino-2-phenylindole) (Cat# P36931; Thermo Fisher Scientific, Grand Island, NY, USA). Imaging was performed under 40× and 60× magnifications on an Olympus BX63 microscope (Olympus, Center Valley, PA, USA), and fluorescence intensity analysis was performed using cellSens Software V2.2 (Olympus, Center Valley, PA, USA).

2.11. Isolating T cells from mouse spleen

Spleens were aseptically harvested and placed in ice-cold 1× MojoSort™ Buffer (BioLegend, San Diego, CA, USA) to preserve cell viability. Tissues were manually dissociated through a 70 μm cell strainer into 15 mL conical tubes. Cell suspensions were centrifuged at 300 ×*g* for 5 min at 4 °C. Supernatants were discarded, and pellets were resuspended in 1 mL Red Blood Cell Lysis Buffer (Thermo Fisher Scientific, Waltham, MA, USA) for 2 min at room temperature. Lysis was quenched with 10 mL MojoSort Buffer, followed by centrifugation and resuspension for downstream applications. $CD4^+$ T cells were isolated from 1–2 × 10^7 splenocytes using the Mouse $CD4^+$ T Cell Isolation Kit (BioLegend, San Diego, CA, USA). Cells were incubated with a Biotin-Antibody Cocktail for 10 min at 4 °C, washed, then treated with Streptavidin Nanobeads for 15 min. The cell mixture was placed in an EasySep™ Magnet (Stemcell Technologies, Vancouver, BC, Canada), and the unlabeled $CD4^+$ T cell fraction was collected. $CD8^+$ T cells were isolated using the Mouse $CD8^+$ T Cell Isolation Kit (Stemcell Technologies, Vancouver, BC, Canada). Cells were incubated with the EasySep™ Selection Cocktail for 10 min, followed by Magnetic Particles for 5 min. Magnetic separation was performed, and the unlabeled $CD8^+$ T cell fraction was collected. All steps were conducted at 4 °C to ensure cell integrity.

2.12. Flow cytometry

Flow cytometry was performed on isolated $CD4^+$ and $CD8^+$ T cells resuspended at 1 × 10^6 cells/100 μL in Cell Staining Buffer (BioLegend, San Diego, CA, USA; Cat# 420201). Live/Dead Fixable Near-IR Viability Dye (Thermo Fisher Scientific, Waltham, MA, USA; Cat# L10119) was added and incubated on ice for 20 min in the dark. After two washes, cells were fixed with Fixation Buffer (BioLegend, San Diego, CA, USA; Cat# 420801) for 15 min at room temperature in the dark. Cells were then blocked with TruStain FcX™ (BioLegend, San Diego, CA, USA; Cat# 101319) for 10 min on ice.

Surface staining was conducted using the following antibodies: Spark UV 387 Rat anti-Mouse CD4 (Clone GK1.5, BioLegend, San Diego, CA, USA; Cat# 100492), Brilliant Violet 605 Rat anti-Mouse CD8a (Clone 53-6.7, BioLegend, San Diego, CA, USA; Cat# 100744), and Brilliant Violet 421 Syrian Hamster anti-Mouse CD28 (Clone 37.51, BioLegend, San Diego, CA, USA; Cat# 102127), following manufacturer protocols. Cells were washed and resuspended in 300 μL for analysis. Samples were acquired using a BD LSRFortessa™ flow cytometer (BD Biosciences, San Jose, CA, USA) and analyzed with FlowJo v10 (BD Biosciences, San Jose, CA, USA). Compensation was performed using single-stained and viability dye-only controls, with appropriate compensation matrices applied. $CD4^+$ and $CD8^+$ T cell subsets were gated and analyzed for CD28 expression. This standardized protocol ensured reproducibility and accuracy using validated reagents and instruments.

2.13. ELISA (Enzyme-Linked Immunosorbent Assay)

Serum levels of Immunoglobulin A (IgA), C-reactive protein (CRP), Interleukin-1β (IL-1β), Interleukin-6 (IL-6), Tumor Necrosis Factor-α (TNF-α), and Interleukin-2 (IL-2) were quantified in experimental mouse groups using commercially available ELISA kits. Mouse IL-1β (Cat# KE10003), IL-6 (Cat# KE10007), and TNF-α (Cat# KE10002) kits were obtained from ProteinTech Group Inc. (Rosemont, IL, USA). The mouse IL-2 ELISA Kit - Quantikine (Cat# M2000) and mouse CRP ELISA kit (Cat# MCRP00) were procured from R&D Systems, Inc. (Minneapolis, MN, USA). The mouse IgA ELISA kit (Cat# ab157717) was acquired from Abcam Limited (Waltham, MA, USA). Serum concentrations of heat shock protein 70 (Hsp70/HSPA4) were determined using a mouse Hsp70 ELISA kit (Cat# RK06376) purchased from Abclonal Technology (Woburn, MA, USA).

2.14. Quantification of endotoxemia by limulus amebocyte lysate (LAL) assay

The serum endotoxemia/chromogenic endotoxin quantification kit (Cat# A39552) was obtained from Pierce Thermo Fisher Scientific (Rockford, IL, USA). The assay was performed as per the manufacturer's protocol from the serum samples from the experimental mouse groups.

2.15. Quantitative real-time polymerase chain reaction

DNA was extracted from fecal samples using the same standardized protocol as in our microbiome sequencing workflow. DNA quality and concentration were assessed to confirm suitability for downstream analysis. Quantitative real-time PCR (qRT-PCR) was performed using SsoAdvanced SYBR Green Supermix (Bio-Rad, Hercules, CA, USA) on a CFX96 thermal cycler (Bio-Rad). Primer sets were gene-specific and individually optimized. Amplification was monitored in real time, and

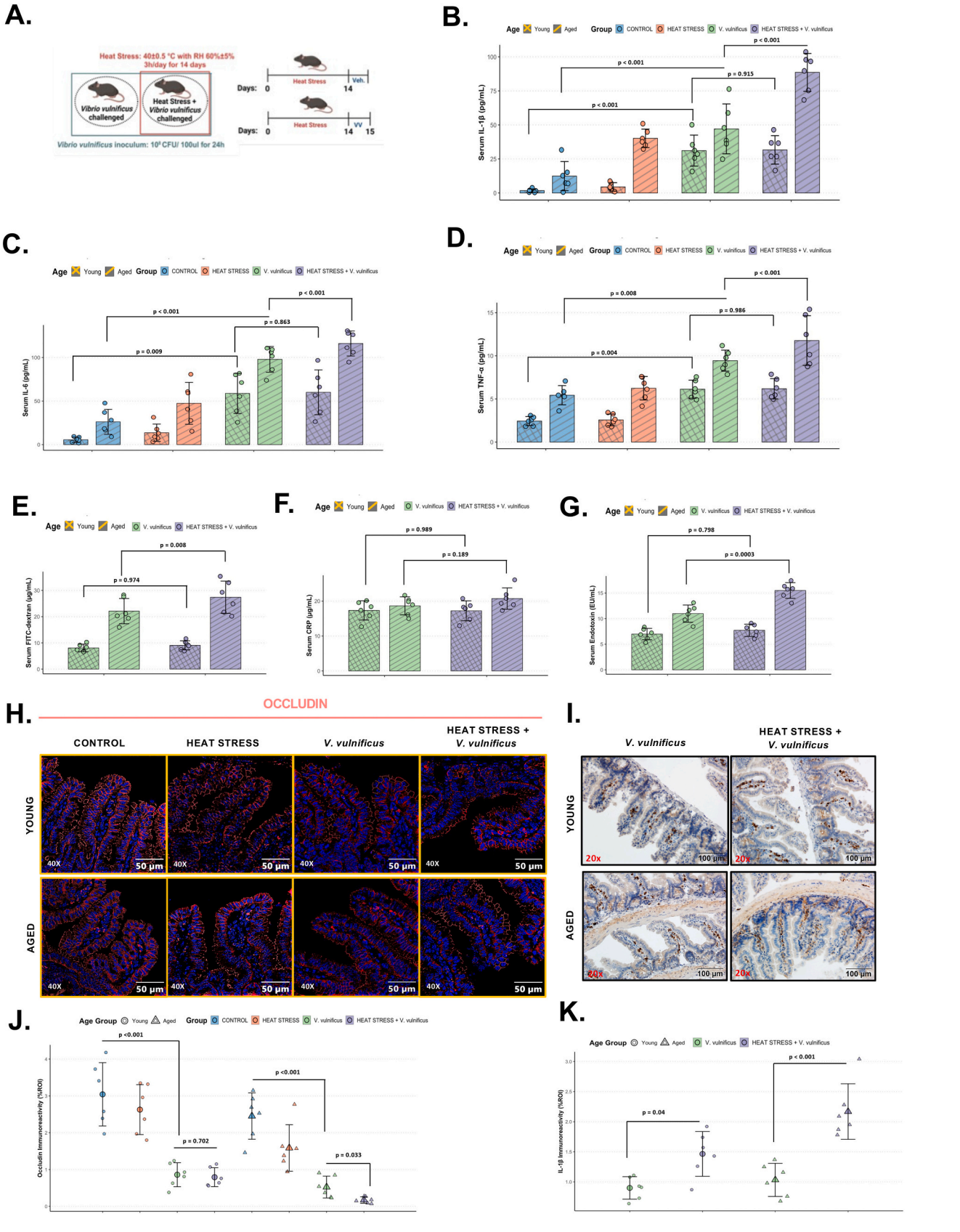

(caption on next page)

Fig. 2. Heat stress exacerbated *Vibrio vulnificus* infection severity in aged mouse model. A. Experimental design for evaluating the impact of heat stress on *Vibrio vulnificus* infection in young (12-week-old) and aged (24-month-old) mice. Mice were subjected to periodic heat stress for two weeks, followed by a single intragastric inoculation of *Vibrio vulnificus* (10^8 CFU/100 μL PBS). Samples were collected 24 h post-infection. B-D. Levels (pg/mL) of serum cytokines IL-1β (B), IL-6 (C), and TNF-α (D) displayed as bar plots with individual data points. Each bar represents the group mean, and error bars depict standard deviation (SD). Data are derived from $n = 6$ biological replicates, with each replicate averaged from three technical replicates. Statistical analysis was conducted using one-way ANOVA to evaluate differences across groups, followed by pairwise post hoc comparisons with Benjamini-Hochberg correction for multiple testing. The significance threshold was set at $p < 0.05$. E. Serum FITC-dextran levels representing intestinal permeability, shown as bar plots with individual points. Bars represent the mean, and error bars indicate SD ($n = 6$ biological replicates, each averaged from three technical replicates). Statistical analysis was performed using one-way ANOVA followed by Benjamini-Hochberg corrected post hoc tests ($p < 0.05$). F. Serum CRP levels displayed as bar plots with individual data points. Bars represent the mean, and error bars indicate SD ($n = 6$ biological replicates, each averaged from three technical replicates). Statistical analysis was performed using one-way ANOVA followed by Benjamini-Hochberg corrected post hoc tests ($p < 0.05$). G. Serum endotoxin levels (EU/mL) displayed as bar plots with individual data points. Bars represent the mean, and error bars indicate SD ($n = 6$ biological replicates, each averaged from three technical replicates). Statistical analysis was performed using one-way ANOVA followed by Benjamini-Hochberg corrected post hoc tests ($p < 0.05$). H, J. Immunofluorescence images of intestinal tight junction protein occludin (H) at 40× magnification (scale bar = 50 μm) and quantification (J) presented as scatter plots with individual data points. Quantification was based on fluorescence intensity from 12 distinct microscopic fields per group ($n = 6$ biological replicates). Statistical analysis was conducted using one-way ANOVA followed by Benjamini-Hochberg corrected post hoc tests ($p < 0.05$). I, K. Immunohistochemistry images of intestinal IL-1β (I) at 20× magnification (scale bar = 100 μm) and quantification (K) presented as scatter plots with individual data points. Quantification was based on immunoreactivity from 12 distinct microscopic fields per group ($n = 6$ biological replicates). Statistical analysis was conducted using one-way ANOVA followed by Benjamini-Hochberg corrected post hoc tests ($p < 0.05$). Pairwise group comparisons (e.g., Control vs. Heat Stress, Infection vs. Heat Stress + Infection) were performed, and adjusted p-values are reported based on the Benjamini-Hochberg correction. Statistical significance was set at $p < 0.05$ for all analyses.

threshold cycle (CT) values were determined with high accuracy. To detect *Vibrio vulnificus*, primers targeting the *VvhA* (hemolysin A) gene were used, following a validated method for clinical and environmental samples. The primer sequences were forward 5′-TTCCAACTTCAAACCGAACTATGA-3′ and reverse 5′-ATTCCAGTCGATGCGAATACGTTG-3′. Universal 16S rRNA gene primers, previously validated by our group and others, were used for bacterial quantification. (Bose et al., 2022), were used, with the sequences 5′-GGGCTACACACGYGCWAC-3′ (forward) and 5′-GACGGGCGGTGTGTRCA-3′ (reverse). Species-specific primers targeting the 16S rRNA gene were used to quantify key gut bacterial taxa. *Akkermansia muciniphila* was detected using forward 5′-CAGCACGTGAAGGTGGGGAC-3′ and reverse 5′-CCTTGCGGTTGGC TTCAGAT-3′ primers (Dingemanse et al., 2015), *Roseburia intestinalis* was quantified using 5′-AGGAGGAAGCCACGGCTAA-3′ (forward) and 5′-TTCCCCACATTGGCCTTTAA-3′ (reverse) primers (Kundra et al., 2024). For *Bifidobacterium pseudolongum*, species-specific primers were 5′-CRATYGTCAAGGAACTYGTGGCCT-3′ (forward) and 5′-GCTGCGAMGAKACCTTGCCGCT-3′ (reverse) (Centanni et al., 2018). Relative abundance was calculated using the ΔCt method, normalized to universal 16S rRNA levels. All reactions were performed in technical triplicates, and average CT values were used for analysis. Negative controls were included in every run to ensure no contamination. This methodology enabled sensitive and specific detection of bacterial species in murine fecal DNA.

2.16. Statistical analyses

Data analysis was conducted using R (v3.6.3) and GraphPad Prism (v10.1.0; GraphPad Software, San Diego, CA, USA). Operational taxonomic units (OTUs) and antibiotic resistance gene counts were normalized via DESeq2, log-transformed, and analyzed using Bray-Curtis dissimilarity and PERMANOVA (vegan package). Principal coordinate analysis (PCoA) and Chao1 α-diversity (fossil package) were computed, and visualizations generated using ggplot2. Welch's two-sample *t*-test (t.test function, base R) assessed differences between two groups. For >2 groups, one-way ANOVA (aov function) with Tukey's HSD post hoc test (multcomp package) was used. Two-way ANOVA and residual diagnostics assessed interactions. Linear mixed-effects models (lme4 package) accounted for repeated measures and inter-individual variability, with model selection guided by AIC. Fixed/random effect significance was tested via likelihood ratio tests, and post hoc comparisons used estimated marginal means (emmeans package). Additional tests including unpaired *t*-tests and one-way ANOVA with Bonferroni-Dunn correction were run in Prism. Assumptions were verified using Shapiro-Wilk (normality) and Levene's (variance) tests. Significance was set at $p < 0.05$. Data are presented as mean ± SD or SEM with *p*-values specified per dataset.

3. Results

3.1. Development and characterization of the periodic heat stress-induced mouse model revealing age-related physiological and immunopathological changes

To establish a murine model of periodic heat stress, 24-month-old and 12-week-old male C57BL/6J wild-type mice were exposed to heat stress under the appropriate conditions described in methods section (Fig. 1A). Rectal temperature, body weight, and food intake were periodically monitored throughout the experiment. A linear mixed-effects model (LME) with ANOVA revealed no significant main effects of group or timepoint on rectal temperature or body weight, nor was the group × timepoint interaction significant. However, food intake exhibited a significant group × timepoint interaction, though neither group nor timepoint alone had a significant effect. Tukey's post hoc tests confirmed no significant pairwise differences for rectal temperature or body weight. Rectal temperature remained stable across groups and timepoints, reflecting effective thermoregulation in all mice. A slight upward trend was observed in the aged heat stress group from Week 1 onward compared to the aged control group ($p = 0.32$, Fig. 1B). Baseline body weight was higher in aged mice compared to young adults. Body weight remained stable across groups, with no statistically significant changes observed ($p = 0.12$, Fig. 1C). Baseline food intake was slightly higher in young adults compared to aged mice. However, a notable decline in food intake was observed in the aged heat stress group during week 1 and week 2, suggesting increased age-related sensitivity to heat stress ($p = 0.049$, Fig. 1D). Heat shock protein 70 (Hsp70), a critical stress responder to heat stress that modulates systemic and intestinal immune responses (Siddiqui et al., 2020), (Victor, 1988), (Hassan et al., 2019), was significantly elevated in the serum of aged heat-stressed groups compared to controls ($p = 0.0427$, Suppl. 1C), as measured by ELISA. Immunofluorescence analysis (green, counterstained with DAPI) further revealed significantly increased intestinal Hsp70 secretion in the aged heat stress group ($p = 0.003$, Suppl. 1A, B), confirming the successful induction of periodic heat stress. In young mice, heat stress significantly increased serum FITC-dextran levels compared to controls ($p = 0.0483$, Fig. 1E), indicating compromised intestinal barrier integrity. CRP levels showed no significant difference between groups ($p = 0.161$, Fig. 1F), while serum endotoxin levels were modestly elevated in heat-stressed mice ($p = 0.0423$, Fig. 1G). Immunohistochemical analysis revealed a significant increase in intestinal IL-1β immunoreactivity in heat-stressed young mice compared to controls ($p = 0.0324$, Fig. 1H, I), highlighting localized inflammatory responses. In aged mice, heat stress

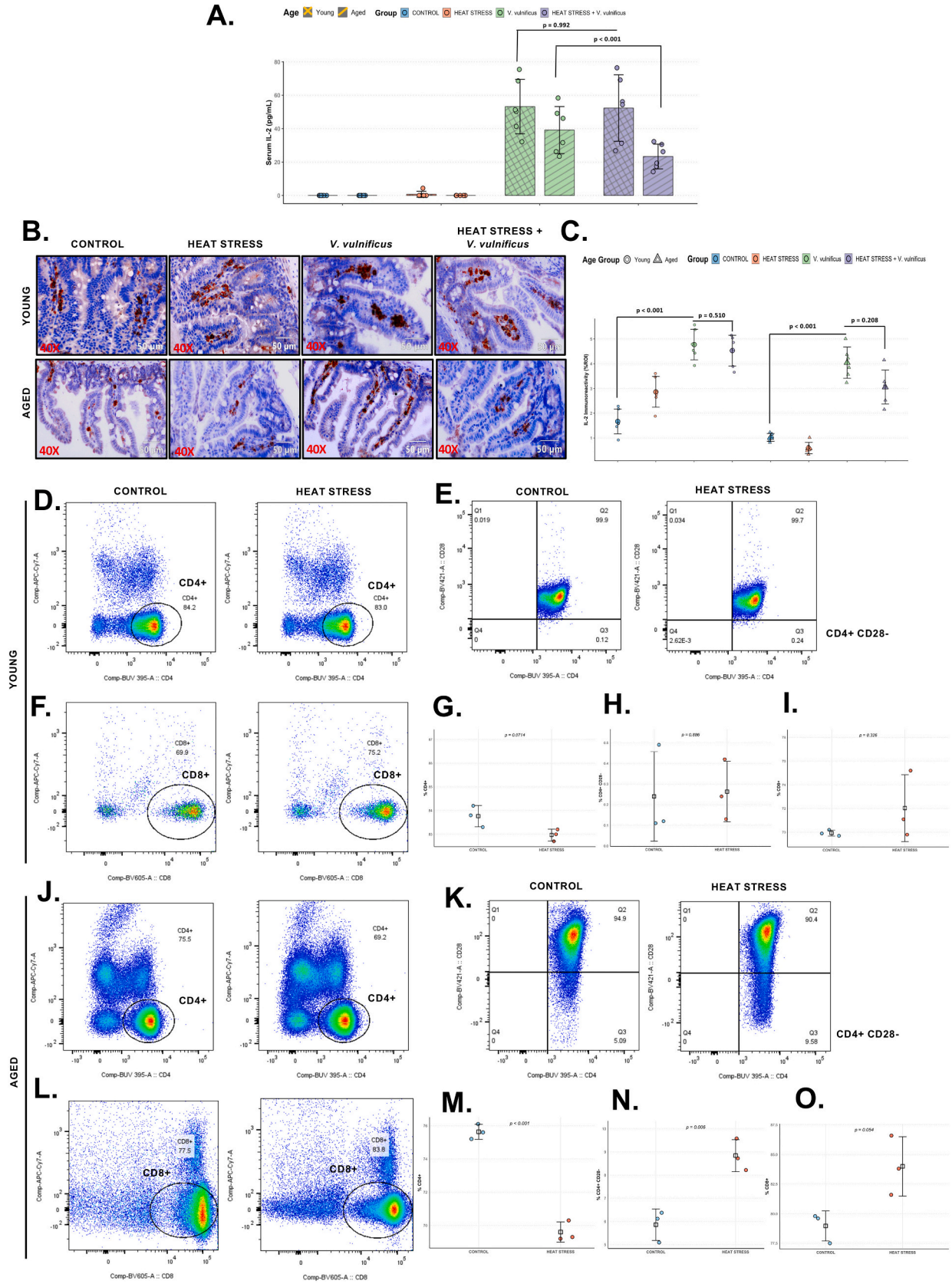

(caption on next page)

Fig. 3. Aggravated infection severity in aging mice due to heat stress-accelerated T-cell immunosenescence under combined stressors.
A. Serum IL-2 levels, predominantly secreted by CD4+ T cells, were quantified via ELISA and are displayed as bar plots with individual data points ($n = 6$ biological replicates, each averaged from three technical replicates). Bars represent group means, with error bars indicating standard deviation (SD). Statistical significance was determined using one-way ANOVA followed by Benjamini-Hochberg corrected post hoc tests ($p < 0.05$). B. Representative immunohistochemistry images of intestinal IL-2 expression for each treatment group in both young and aged cohorts, captured at 40× magnification (scale bar = 50 μm). C. Quantification of intestinal IL-2 immunoreactivity in young (12-week-old) and aged (24-month-old) mice is presented as scatter plots ($n = 6$ biological replicates, each averaged from three technical replicates). Bars represent group means with SD error bars. Statistical analysis was conducted using one-way ANOVA with Benjamini-Hochberg corrected post hoc tests ($p < 0.05$). D-F. Representative flow cytometry density plots illustrate gating strategies and the percentage of CD4+ T cells (percent of parent population) (D), CD4 + CD28− T cells (percent of parent population) (E), and CD8+ T cells (percent of parent population) (F) in young mice, comparing control and heat stress groups. Quadrants represent population distributions: Q1 (negative for both markers), Q2 (positive for the primary marker), Q3 (double-negative population), and Q4 (double-positive population). Percentages indicate cell populations in respective quadrants as percent of parent population. G-I. Quantification of CD4+ T cells (G), CD4 + CD28− T cells (H), and CD8+ T cells (I) across treatment groups in young mice is presented as scatter plots with individual data points ($n = 3$ biological replicates, each averaged from three technical replicates). Data are expressed as mean ± 95 % confidence interval (CI). Statistical analysis was conducted using an unpaired, two-tailed *t*-test with Benjamini-Hochberg correction ($p < 0.05$). J-L. Flow cytometry density plots for aged mice illustrate gating strategies and percentages of CD4+ T cells (percent of parent population) (J), CD4 + CD28− T cells (K), and CD8+ T cells (L) in control and heat stress groups as percent of parent population. Quadrants represent population distributions: Q1 (negative for both markers), Q2 (positive for the primary marker), Q3 (double-negative population), and Q4 (double-positive population). Percentages indicate cell populations in respective quadrants (percent of parent population). M-O. Quantification of CD4+ T cells (percent of parent population) (M), CD4 + CD28− T cells (percent of parent population) (N), and CD8+ T cells (percent of parent population) (O) in aged mice is shown as scatter plots ($n = 3$ biological replicates, each averaged from three technical replicates). Data are expressed as mean ± 95 % confidence interval (CI). Statistical analysis was conducted using an unpaired, two-tailed *t*-test with Benjamini-Hochberg correction ($p < 0.05$).

had more pronounced systemic effects. Serum FITC-dextran levels were significantly elevated in the heat stress group compared to controls ($p = 0.0228$, Fig. 1J), as were CRP levels ($p = 0.012$, Fig. 1K) and endotoxin levels ($p = 0.0102$, Fig. 1L). Immunohistochemical analysis revealed markedly higher IL-1β levels in the intestines of heat-stressed aged mice ($p = 0.0123$, Fig. 1M, N), reflecting heightened inflammatory responses and severe intestinal barrier dysfunction. Overall, heat stress induced significant intestinal barrier dysfunction and systemic inflammation in both young and aged mice. However, aged mice exhibited greater variability in rectal temperature, more severe intestinal barrier disruption, and higher inflammatory responses compared to their younger counterparts. These findings underscore the age-dependent effects of periodic heat stress on physiological and immunopathological markers.

3.2. Heat stress exacerbated *Vibrio vulnificus* infection severity in aged mouse model

To assess the impact of heat stress on the severity of *Vibrio vulnificus* infection in young (12-week-old) and aged (24-month-old) mice, animals were inoculated with intragastric infection of *Vibrio vulnificus* after heat stress exposure. The study concluded 24 h post-infection (Fig. 2A). Fecal DNA analysis confirmed infection through qRT-PCR detection of the VvhA gene, which was consistently present in infected groups at 12- and 24-hour post-infection (Suppl. Fig. 2A). The immune response was evaluated by measuring two key pro-inflammatory cytokines, IL-1β and TNF-α, both associated with *Vibrio vulnificus* infection (Shin et al., 2002), (Qin et al., 2019). In young mice, IL-1β and TNF-α levels did not differ significantly between the heat stress plus infection and infection-only groups ($p = 0.915$ and $p = 0.986$, respectively; Fig. 2B, D). In contrast, aged mice exhibited a significant synergistic increase in both IL-1β ($p < 0.001$, Fig. 2B) and TNF-α ($p < 0.001$, Fig. 2D) under dual exposure conditions compared to the infection-only group. IL-6, a pleiotropic cytokine associated with *Vibrio vulnificus* infection (Shin et al., 2002), showed a significant increase in the heat stress plus infection group compared to the infection-only group in aged mice ($p < 0.01$, Fig. 2C), while no changes were observed in young mice ($p = 0.986$, Fig. 2C). However, IL-6 levels were elevated in the infection-only group compared to controls in both age groups ($p < 0.001$, Fig. 2C). Intestinal permeability, assessed by serum FITC-dextran levels, was significantly elevated in aged heat stress plus infection mice compared to infection-only mice ($p = 0.008$, Fig. 2E), while no significant differences were observed in young mice ($p = 0.974$, Fig. 2E). Baseline FITC-dextran levels were higher in aged mice, and the increase under dual exposure conditions was more pronounced. Gut barrier integrity was further evaluated by analyzing the expression of the tight junction protein occludin via immunofluorescence. In young mice, occludin expression remained unchanged in the heat stress plus infection group compared to infection-only mice ($p = 0.702$, Fig. 2H, J). However, aged mice exhibited significant occludin disruption under dual exposure conditions, with decreased expression in the heat stress plus infection group compared to infection-only mice ($p = 0.033$, Fig. 2H, J). Systemic inflammation, assessed by serum CRP levels, remained unchanged in the heat stress plus infection group compared to the infection-only group in both young ($p = 0.989$, Fig. 2F) and aged mice ($p = 0.189$, Fig. 2F). However, a marginal trend toward elevated CRP levels was observed in aged mice under dual exposure conditions, suggesting a heightened inflammatory response compared to young mice. Serum endotoxin levels, indicative of endotoxemia, were significantly elevated in aged heat stress plus infection mice compared to infection-only mice ($p = 0.0003$, Fig. 2G), whereas no significant changes were observed in young mice ($p = 0.798$, Fig. 2G). Immunohistochemical analysis revealed elevated intestinal IL-1β levels in the heat stress plus infection group compared to the infection-only group in both young ($p = 0.04$, Fig. 2I, K) and aged mice ($p < 0.001$, Fig. 2I, K), with a more pronounced effect in aged mice. These results demonstrate that heat stress amplifies the severity of *Vibrio vulnificus* infection, with aged mice showing heightened responses. Compared to young mice, aged mice exhibited greater systemic inflammation, more severe intestinal barrier disruption, and elevated markers of intestinal inflammation.

3.3. Aggravated infection severity in aging mice due to heat stress-accelerated T-cell immunosenescence under combined stressors

In both young and aged mice, serum IL-2 levels were significantly elevated in the *V. vulnificus* and heat stress + *V. vulnificus* groups, reflecting a robust immune response to infection. In young mice, no significant difference was observed between the *V. vulnificus* and heat stress + *V. vulnificus* groups ($p = 0.992$, Fig. 3A), indicating that heat stress did not further amplify IL-2 production in the presence of infection. Conversely, in aged mice, serum IL-2 levels were significantly lower in the heat stress + *V. vulnificus* group compared to the *V. vulnificus* group ($p = 0.0005$, Fig. 3A), suggesting an antagonistic interaction between heat stress and infection in aged animals. Comparative analyses within age-group revealed age-dependent differences in IL-2 production, with aged mice displaying significantly lower serum IL-2 levels than young mice under heat stress + *V. vulnificus* condition when compared to *V. vulnificus* infection-only group, indicating a dysregulated IL-2 response in aged animals under combined effects of heat stress and infection. Intestinal IL-2 expression, evaluated through immunohistochemistry, showed similar patterns. In young mice, IL-2 expression was significantly elevated in the *V. vulnificus* and heat stress + *V. vulnificus* groups compared to the control ($p < 0.001$,

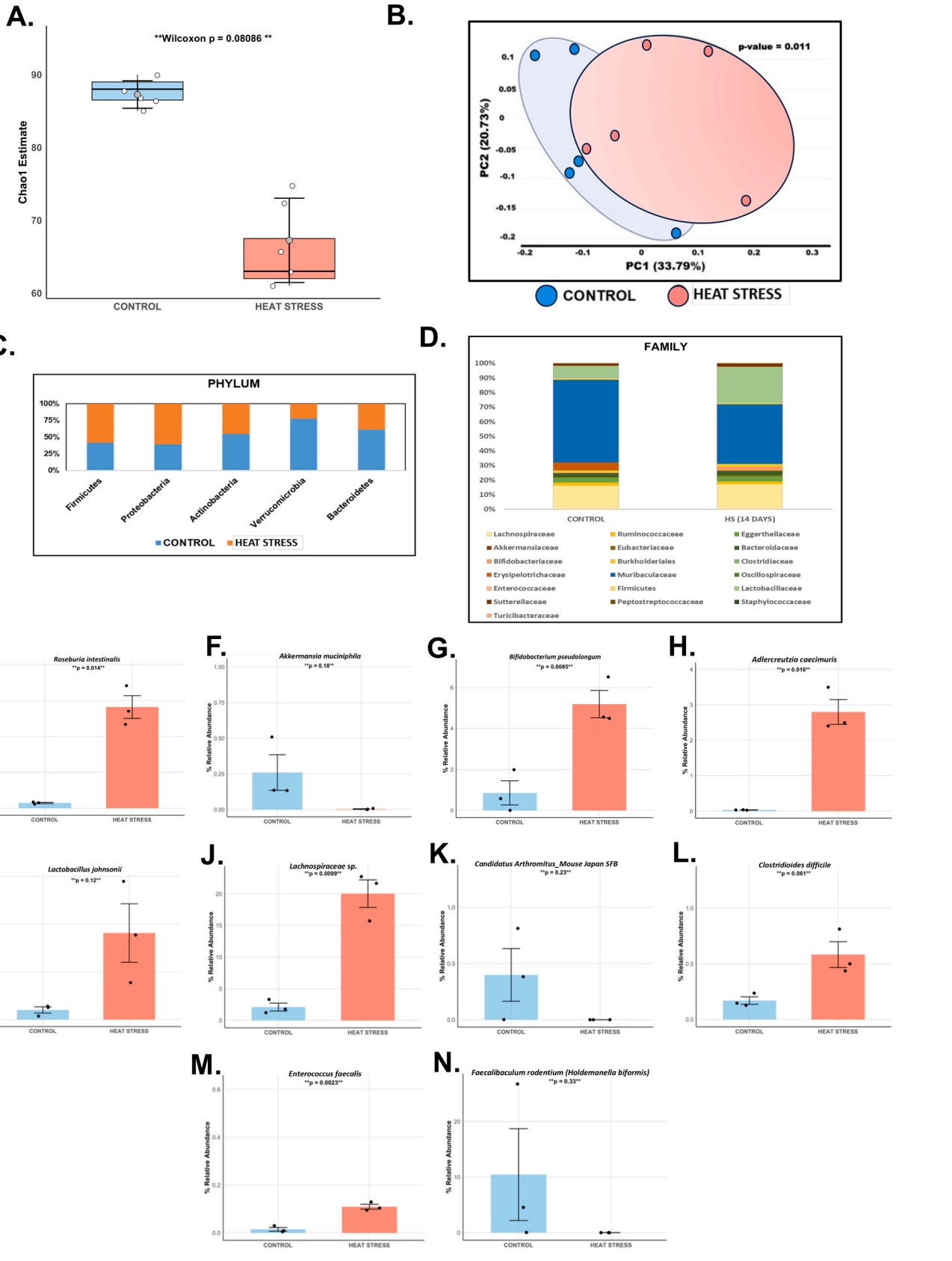

(caption on next page)

Fig. 4. Heat stress-induced gut microbiome alterations. A. Box plots depicting α-diversity (Chao1 index) in fecal samples from control and heat stress groups in aged mice ($n = 5$ biological replicates per group). Statistical significance was assessed using the Wilcoxon rank-sum test, with Benjamini-Hochberg correction applied for multiple comparisons ($p < 0.05$). B. Principal Coordinate Analysis (PCoA) representing microbial β-diversity (Bray-Curtis dissimilarity) in fecal samples from control and heat stress groups in aged mice ($n = 5$ biological replicates per group). The plot displays PC1 (33.79 % variance) and PC2 (20.73 % variance), showing distinct clustering of microbial communities. Statistical analysis was performed using permutational multivariate analysis of variance (PERMANOVA), with significance determined at a threshold of $p < 0.05$. C. Bar plots showing the relative abundance (%) of dominant phyla in the gut microbiota of aged mice under control and heat stress conditions ($n = 5$ biological replicates per group). D. Bar plots representing the relative abundance (%) of selected bacterial families in the gut microbiota of aged mice under control and heat stress conditions ($n = 5$ biological replicates per group). E-I. Bar plots showing the differential abundances of key microbial species in aged mice, with individual data points represented (n = 3 biological replicates). Each panel illustrates specific taxa as follows: E. *Roseburia intestinalis*, F. *Akkermansia muciniphila*, G. *Bifidobacterium pseudolongum*, H. *Adlercreutzia caecimuris*, I. *Lactobacillus johnsonii*, J. *Lachnospiraceae* sp., K. *Candidatus Arthromitus_Mouse Japan SFB*, L. *Clostridioides difficile*, and M. *Enterococcus faecalis*, N. *Fecalibaculum rodentium*. Statistical comparisons for species-level data were performed using the Statistical analysis was conducted using an unpaired, two-tailed *t*-test with Benjamini-Hochberg correction ($p < 0.05$). Bars indicate group means, with error bars representing standard deviation (SD).

Fig. 3B, C), with no significant difference between the *V. vulnificus* and heat stress + *V. vulnificus* groups ($p = 0.510$). In aged mice, a slight reduction in intestinal IL-2 expression was observed in the *V. vulnificus* and heat stress + *V. vulnificus* group compared to the *V. vulnificus* group ($p = 0.208$, Fig. 3B, C), although this decrease was not statistically significant. These findings highlight age-dependent modulation of IL-2 responses, with distinct immune alterations observed in aged animals under combined heat stress and infection conditions. Flow cytometry analysis of splenic T-cell populations revealed significant differences across treatment groups, emphasizing age-dependent effects of heat stress on immune dynamics. Gating strategies for flow cytometric analysis were rigorously established prior to experimentation (Suppl. Fig. 3A, B). In young mice, CD4+ T-cell proportions were unaffected by heat stress compared to the Control group ($p = 0.071$, Fig. 3D, G). However, aged mice exposed to heat stress showed a significant reduction in CD4+ T-cell proportions ($p < 0.001$, Fig. 3J, M), indicating an age-related decline in CD4+ T-cell populations under stress conditions. Heat stress significantly increased CD4 + CD28− T-cell proportions, a hallmark of immunosenescence, particularly in aged mice. Aged mice exposed to heat stress had significantly higher CD4 + CD28− T-cell proportions compared to controls ($p = 0.006$, Fig. 3K, N), while no significant changes were observed in young mice ($p = 0.886$, Fig. 3E, H). This highlights an age-dependent susceptibility to stress-induced immunosenescence. CD8+ T-cell proportions, representing cytotoxic T-cell populations, remained stable across treatment groups in young mice ($p = 0.326$, Fig. 3F, I). In aged mice, however, CD8+ T-cell proportions were markedly increased following heat stress exposure ($p = 0.05$, Fig. 3L, O), suggesting heightened inflammatory potential in cytotoxic T cells under stress conditions. To further validate systemic findings, T-cell immunosenescence was assessed in the intestinal microenvironment. Immunohistochemical staining of CD28 in intestinal sections from aged mice revealed a significant reduction in CD28 expression under heat stress ($p = 0.011$, Suppl. Fig. 4A, C). Immunofluorescence analysis showed a parallel decrease in CD4+ T-cell reactivity in the intestine of heat stress-exposed aged mice compared to controls ($p = 0.036$, Suppl. Fig. 4B, D). Besides, in aged mice the serum IgA levels, marker of immunosenescence was found to be elevated under heat stress condition when compared to the control ($p = 0.0248$, Suppl. Fig. 4E). These results suggested that heat stress accelerates T-cell aging at both systemic and intestinal levels in aged mice, underscoring a comprehensive impact of environmental stressors on immune aging.

3.4. Heat stress induced gut microbiome alterations

Comprehensive metagenomic analysis revealed significant alterations in the gut microbiota under heat stress exposure. Alpha diversity, assessed via the Chao1 index, showed a decline in microbial richness in the heat stress group compared to controls, although this decrease did not reach statistical significance ($p = 0.08$, Fig. 4A). Beta diversity, visualized through Principal Coordinate Analysis (PCoA) of Bray-Curtis dissimilarity, demonstrated significant separation between the groups, with clustering explained by 33.79 % and 20.73 % of the total variance along PC1 and PC2, respectively ($p = 0.011$, Fig. 4B). Additionally, a temporal microbiome analysis of the aged heat stress group at baseline (day 0), 7 days, and 14 days of exposure to periodic heat stress revealed distinct microbial shifts. Beta diversity, assessed via PCoA of Bray-Curtis dissimilarity, showed distinct clustering across timepoints, with 40.19 % and 18.5 % of variance explained by PC1 and PC2, respectively (baseline vs day 7: $p = 0.05$; baseline vs day 14: $p = 0.05$; day 7 vs day 14: $p = 0.02$, Suppl. Fig. 5B). In contrast, Chao1 alpha diversity showed a nonsignificant decreasing trend over time ($p > 0.05$, Suppl. Fig. 5B). These findings indicated that heat stress induced distinct shifts in the composition of the gut microbiota. At the phylum level, heat stress caused substantial changes in microbial community structure. The relative abundance of *Verrucomicrobia*, *Bacteroidetes*, and *Actinobacteria* was notably reduced, while *Firmicutes* and *Proteobacteria*, phyla often associated with dysbiosis, were significantly enriched in the heat stress group compared to controls (Fig. 4C). Similarly, analysis at the family level revealed marked changes in key bacterial families, with reductions in beneficial commensals and increases in taxa linked to opportunistic pathogens (Fig. 4D). At the species level, specific taxa were significantly altered under heat stress conditions. The butyrate-producing bacterium *Roseburia intestinalis* was significantly altered ($p = 0.014$, Fig. 4E), as were *Bifidobacterium pseudolongum* ($p = 0.008$, Fig. 4G), *Adlercreutzia caecimuris* ($p = 0.016$, Fig. 4H), and *Lachnospiraceae* species ($p = 0.009$, Fig. 4J), which are critical for maintaining gut homeostasis. *Lactobacillus johnsonii*, a key probiotic species, showed marked alteration ($p = 0.12$, Fig. 4I). Conversely, *Enterococcus faecalis*, an opportunistic pathogen associated with inflammation, was significantly elevated in the heat stress group ($p = 0.002$, Fig. 4M). Although not statistically significant, other notable changes included reductions in *Akkermansia muciniphila* ($p = 0.18$, Fig. 4F), a mucin-degrading bacterium with anti-inflammatory properties, and *Candidatus Arthromitus_Mouse Japan SFB* ($p = 0.23$, Fig. 4K), a segmented filamentous bacterium involved in immune regulation. Additionally, *Clostridioides difficile*, a pathogen linked to antibiotic-associated colitis, showed an increased abundance ($p = 0.18$, Fig. 4L), while *Fecalibaculum rodentium*, a commensal bacterium promoting gut health, was reduced ($p = 0.18$, Fig. 4N). These results underscored the profound impact of heat stress on the gut microbiome of aged mice, leading to decreased diversity and compositional changes favoring dysbiosis. The observed alterations in key bacterial taxa highlight the disruption of gut homeostasis and suggest a potential link between heat stress and increased vulnerability to inflammatory conditions in aging populations.

3.5. Functional mapping revealed microbial candidates, including Akkermansia muciniphila, linked to heat stress-exacerbated vibriosis severity in aged mice, validated through gut depletion and supplementation models

The network analysis identified bacteria species like *Roseburia intestinalis* and *Bifidobacterium pseudolongum* can be important in mitigating inflammatory burden and T-cell dynamics, primarily through short-chain fatty acid (SCFA) production and *Akkermansia muciniphila*

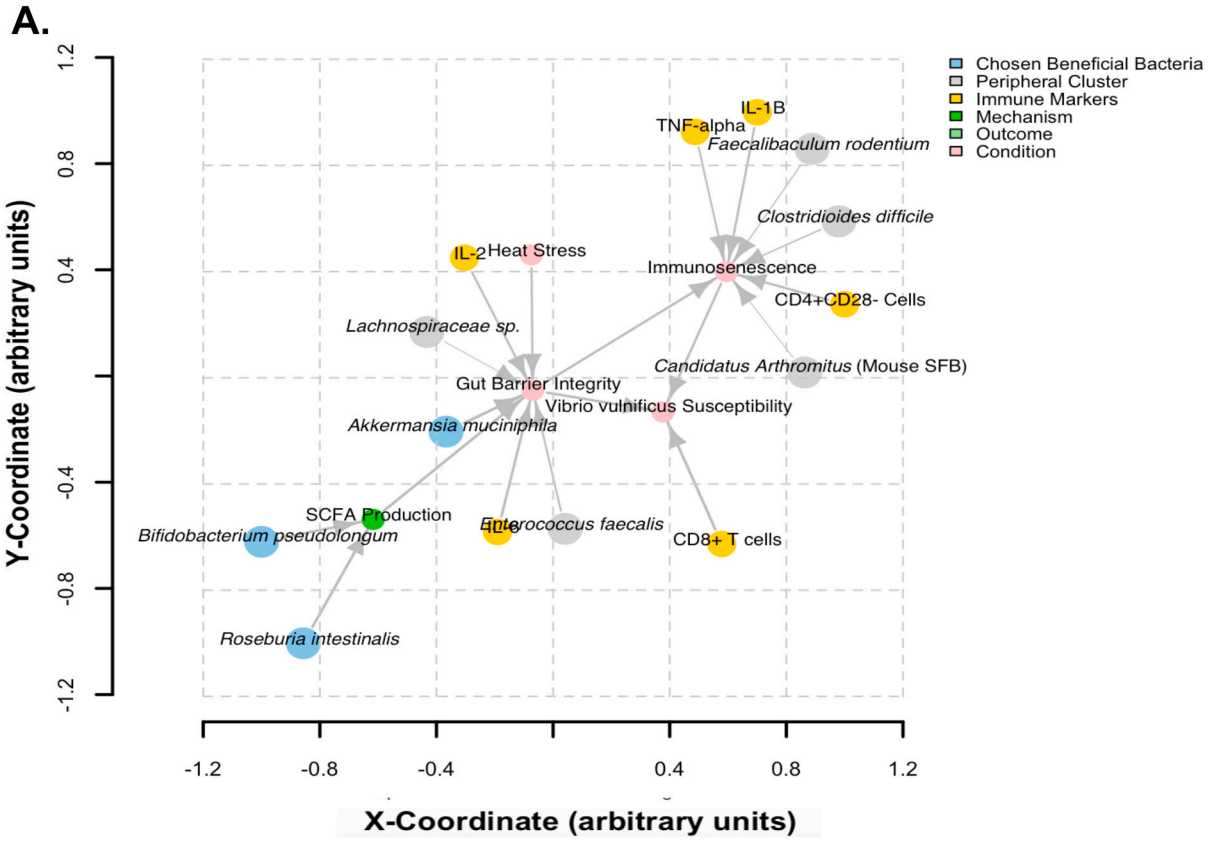

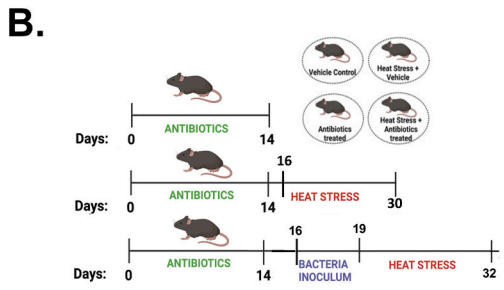

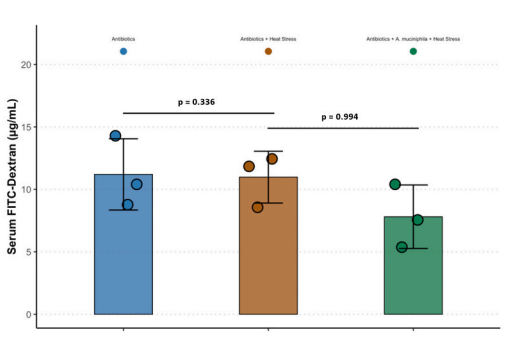

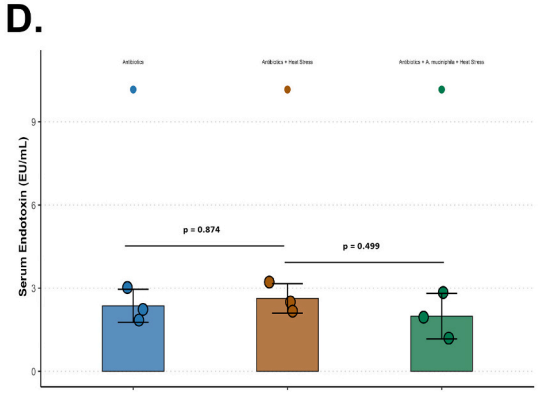

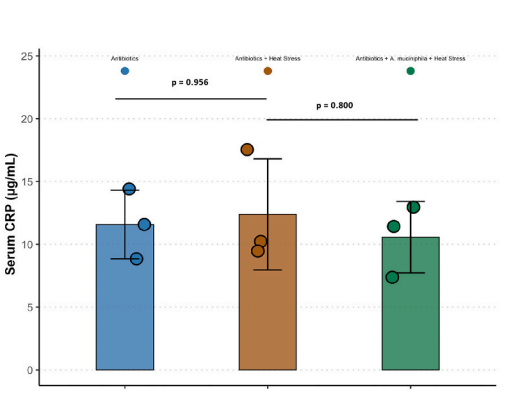

(caption on next page)

Fig. 5. Functional mapping revealed microbial candidates, including *Akkermansia muciniphila*, linked to heat stress-exacerbated vibriosis severity in aged mice, validated through gut depletion and supplementation models. A. Functional network illustrating the relationships among bacterial species, immune markers, and gut barrier integrity under heat stress conditions in aged mice. The network included primary bacterial species (*Roseburia intestinalis*, *Bifidobacterium pseudolongum*, *Akkermansia muciniphila*), peripheral bacterial species (*Clostridioides difficile*, *Enterococcus faecalis*, and others), immune markers (e.g., IL-1B, IL-6, TNF-alpha, IL-2, CD8+ T cells, CD4 + CD28- cells), and functional outcomes such as SCFA production, gut barrier integrity, and immunosenescence. Data sources included the KEGG database, MicrobiomeDB, and PubMed. Relationships were visualized using weighted edges derived from published evidence, and the network was organized using a Fruchterman-Reingold layout. Axis units were scaled, and dashed grid lines were incorporated to improve interpretability. B. Schematic of the experimental design for evaluating the role of specific gut microbial species in mitigating heat stress-induced immunopathology, a murine model was developed combining antibiotic-mediated gut microbiota depletion, single microbial species reconstitution, and heat stress exposure. C. Serum FITC-Dextran levels across experimental groups. Groups included Antibiotics, Antibiotics + Heat Stress, and Antibiotics + *A. muciniphila* + Heat Stress. Statistical comparisons were performed using one-way analysis of variance (ANOVA) followed by Tukey's post-hoc test, with a significance threshold set at $p < 0.05$. Data are presented as Mean ± standard deviation (SD). D. Serum endotoxin levels across experimental groups. Groups included Antibiotics, Antibiotics + Heat Stress, and Antibiotics + *A. muciniphila* + Heat Stress. Statistical comparisons were performed using one-way analysis of variance (ANOVA) followed by Tukey's post-hoc test, with a significance threshold set at $p < 0.05$. Data are presented as Mean ± standard deviation (SD). E. Serum CRP levels across experimental groups. Groups included Antibiotics, Antibiotics + Heat Stress, and Antibiotics + *A. muciniphila* + Heat Stress. Statistical comparisons were performed using one-way analysis of variance (ANOVA) followed by Tukey's post-hoc test, with a significance threshold set at $p < 0.05$. Data are presented as Mean ± standard deviation (SD). For all, $n = 3$ biological replicates, each averaged from three technical replicates were represented in figures.

for maintaining gut barrier integrity. Peripheral bacterial species, including *Clostridioides difficile* and *Enterococcus faecalis*, were associated with gut barrier dysfunction and immunosenescence. Immune markers such as IL-1β and TNF-α were highlighted as key mediators linking bacterial activity to systemic inflammatory responses. Functional pathway analyses further demonstrated that gut dysbiosis and immune dysfunction under heat stress may contribute to increased susceptibility to *Vibrio vulnificus* infection, underscoring the therapeutic potential of specific bacterial species in maintaining gut and immune health during environmental stress (Fig. 5A). The schematic (Fig. 5B) outlines the experimental framework involving microbiota depletion, microbial reconstitution, and heat stress exposure in aged mice. The aged mice cohorts were pretreated with a broad-spectrum antibiotic cocktail for 14 days to deplete gut microbiota as described in methods, followed by a 2-day recovery interval and heat stress. Previous research from our group validated this protocol's efficacy using whole metagenomic sequencing (Bose et al., 2024). In this study, the model was revalidated by measuring the DNA concentration in fecal samples from both the control and antibiotic-treated groups (Suppl. Fig. 6A). The results showed a significant decrease in DNA concentration in the antibiotic-treated group compared to the control ($p = 0.033$, Suppl. Fig. 6A). Additionally, the global 16S rRNA content was quantified in antibiotic groups in several time points using a gene-specific primer set, revealing a significant increase in C_T value, indicative of decreased 16S rRNA content in the antibiotic-treated group compared to the control ($p = 0.002$, Suppl. Fig. 6B). These findings collectively confirmed the successful establishment of the antibiotic-induced gut depletion model. On Day 16, specific bacterial species identified in the microbiome data, including *Akkermansia muciniphila*, *Roseburia intestinalis*, and *Bifidobacterium pseudolongum*, were reintroduced via oral inoculation at species-specific colony-forming unit (CFU) doses for four consecutive days to facilitate gut colonization. All groups, except the antibiotic control, underwent periodic heat stress from day 19 to day 32. The colonization efficiency of each microbial species was validated with quantitative RT-PCR using species specific 16S rRNA primers (Suppl. Fig. 6C, D, and E). Serum FITC-dextran levels, a marker of intestinal permeability, were measured across the treatment groups: antibiotics-only, antibiotics + heat Stress, and antibiotics + *A. muciniphila* + heat stress. Although no statistically significant differences were observed, a decreasing trend in the antibiotics + *A. muciniphila* + heat stress group compared to the antibiotics + heat stress group ($p = 0.994$, Fig. 5C) suggested that *A. muciniphila* reconstitution marginally improved intestinal barrier integrity under heat stress conditions. Similar trends were observed in serum endotoxin and CRP levels, with marginal reductions in the antibiotics + *A. muciniphila* + heat stress group compared to the antibiotics + heat stress group ($p = 0.499$ and $p = 0.800$, respectively, Figs. 5D, E). These findings indicated that while microbiota depletion followed by reconstitution with *Akkermansia muciniphila* did not significantly modulate intestinal permeability, endotoxemia, or systemic inflammation, it did result in marginal improvements, potentially alleviating heat stress-induced pathophysiology in aged mice. Further investigations were warranted to explore the roles of additional microbial species in mitigating heat stress-exacerbated pathophysiology.

3.6. Modulation of T-cell immunosenescence by probiotics in heat-stressed aged mice

Flow cytometry analysis revealed significant differences in T-cell subpopulations among the aged experimental groups, emphasizing the effects of heat stress and probiotic reconstitution on immune cell dynamics. The CD4+ T cell population showed a significant reduction in the antibiotics + heat stress group compared to the antibiotics-only group ($p = 0.0021$, Fig. 6A, C), highlighting the detrimental impact of heat stress on immune cell populations in the absence of gut microbiota. Probiotic reconstitution mitigated these reductions effectively. Both the antibiotics + *R. intestinalis* + heat stress group ($p = 0.0004$, Fig. 6A, C) and the antibiotics + *B. pseudolongum* + heat stress group ($p = 0.005$, Fig. 6A, C) demonstrated significantly higher CD4+ levels compared to the antibiotics + heat stress group, with no significant differences between the two probiotic groups ($p = 0.9978$, Fig. 6A, C). Neither probiotic group differed significantly from the antibiotics-only group ($p > 0.05$, Fig. 6A, C), indicating restoration of CD4+ levels to baseline. For CD4 + CD28− T cells, a marker of immunosenescence, significant differences were also observed. The antibiotics + heat stress group exhibited a significant increase in CD4 + CD28− proportions compared to the antibiotics-only group ($p = 0.004$, Fig. 6B, D), reflecting exacerbated immunosenescence under heat stress. Probiotic reconstitution significantly reduced CD4 + CD28− levels in the antibiotics + *R. intestinalis* + heat stress group compared to the antibiotics + heat stress group ($p = 0.075$, Fig. 6B, D), whereas the antibiotics + *B. pseudolongum* + heat stress group did not show a significant reduction ($p = 0.979$, Fig. 6B, D). A significant difference between the two probiotic groups ($p = 0.048$, Fig. 6B, D) suggested that *R. intestinalis* was more effective in mitigating CD4+ T-cell immunosenescence. For CD8+ T cells, significant increases were observed in the antibiotics + heat stress group compared to the antibiotics-only group ($p = 0.0024$, Fig. 6E, F), indicating cytotoxic T-cell vulnerability under heat stress. Probiotic reconstitution mitigated this increase effectively. The antibiotics + *B. pseudolongum* + heat stress group exhibited a statistically significant reduction in CD8+ levels compared to the antibiotics + heat stress group ($p = 0.035$, Fig. 6E, F), while the antibiotics + *R. intestinalis* + heat stress group showed a reduction that was not statistically significant ($p = 0.32$, Fig. 6E, F). Neither probiotic group differed significantly from the antibiotics-only group ($p > 0.05$, Fig. 6E, F), suggesting restoration of CD8+ levels to baseline. Overall, *B. pseudolongum* appeared more

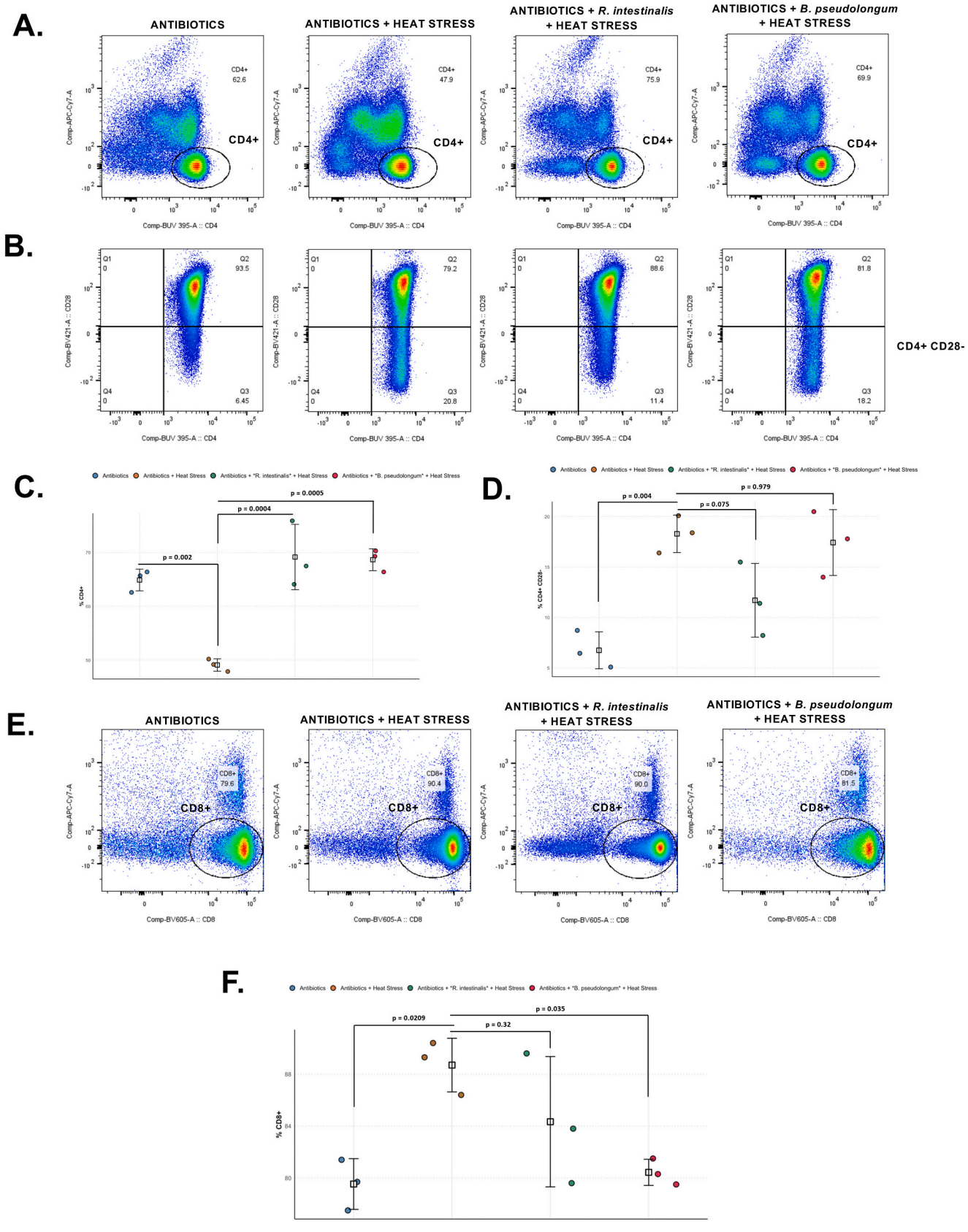

(caption on next page)

Fig. 6. Modulation of T-cell immunosenescence by probiotics in heat-stressed aged mice. A, B, E. Groups included Antibiotics, Antibiotics + Heat Stress, Antibiotics + *R. intestinalis* + Heat Stress, and Antibiotics + *B. pseudolongum* + Heat Stress: representative flow cytometry density plots showing the gating strategy and the percentage of splenic CD4+ T cells (A), CD4 + CD28− T cells (B), and CD8+ T cells (E) represented as percent of parent population. Quadrants represent population distributions: Q1 (negative for both markers), Q2 (positive for the primary marker), Q3 (double-negative population), and Q4 (double-positive population). Percentages indicate cell populations in respective quadrants as a percent of parent population. C, D, F. Quantification of CD4+ T cells (C), CD4 + CD28− T cells (D), and CD8+ T cells (F) in aged mice is shown across groups (Antibiotics, Antibiotics + Heat Stress, Antibiotics + *R. intestinalis* + Heat Stress, and Antibiotics + *B. pseudolongum* + Heat Stress) is presented as scatter plots with individual data points (n = 3 biological replicates, each averaged from three technical replicates). Data are expressed as mean ± 95 % confidence interval (CI). Statistical comparisons were performed using one-way ANOVA followed by Tukey's post hoc test, with a significance threshold set at $p < 0.05$.

effective in regulating CD8+ T-cell populations affected by heat stress. These findings underscore the detrimental effects of heat stress on T-cell populations in aged mice and highlight the therapeutic potential of probiotics, particularly *R. intestinalis* and *B. pseudolongum*, in ameliorating these effects.

3.7. Heat stress modified the composition of host gut-resistome and augmented resistance to clinically relevant antibiotics in aged mice

Heat stress significantly reduced the α-diversity of antibiotic resistance genes (ARGs) within the gut microbiota of aged mice, as indicated by the Chao1 estimate ($p = 0.014$, Fig. 7A). Additionally, β-diversity analysis using Bray-Curtis dissimilarity revealed distinct clustering between the ARG profiles of the control and heat stress groups, as visualized in the Principal Coordinate Analysis (PCoA) plot (PC1 explaining 44.17 % variance and PC2 explaining 31.37 %, $p = 0.02$, Fig. 7B). The network analysis of resistance and virulence genes associated with host gut microbiota revealed distinct associations between virulence, resistance genes, bacterial species, and experimental conditions, highlighting potential interactions in the microbiome under heat stress (Fig. 7C). Key resistance genes, such as tetQ, were strongly associated with *Bacteroides fragilis* and the heat stress condition, suggesting its involvement in adaptive resistance mechanisms. Similarly, virulence gene bmhA demonstrated a significant link with *Bacteroides thetaiotaomicron*, while IS942 was primarily associated with *Bacteroides ovatus* under control conditions. Node centrality analysis showed that tetQ had the highest closeness centrality, emphasizing its central role in the network, followed by bmhA and IS942. Edge weights, represented by width and color intensity, highlighted the strength of interactions, with the most robust connections observed under heat stress conditions. This suggested that environmental stressors such as heat stress modulate microbial community interactions, promoting the expression of resistance genes. The spatial arrangement of nodes, based on the Fruchterman-Reingold layout, provided a clear visualization of the relationships. Bacterial species clustered with their respective virulence genes, further confirming the specificity of associations. These findings underlined the potential of the gut microbiome to adapt to environmental stress by modulating virulence and resistance gene expression. Heat stress induced a selective enrichment of clinically significant ARGs. Notably, resistance genes against tetracycline (*tetr*) were significantly elevated in the heat stress group compared to controls ($p = 0.036$, Fig. 7D). Although vancomycin resistance genes (*vanr*) exhibited a pronounced increase, this change did not reach statistical significance ($p = 0.15$, Fig. 7F). In contrast, ARGs conferring resistance to aminoglycosides (*amer*, $p = 0.935$, Fig. 7E) and macrolides (*msr*, $p = 0.86$, Fig. 7G) showed no significant differences between the groups. These findings collectively highlighted the selective pressure of heat stress on the gut resistome, leading to a distinct ARG profile with potential clinical implications, particularly concerning tetracycline and vancomycin resistance, in aging mice.

4. Discussion

This study is the first to investigate the interplay between heat stress, aging, the gut microbiome, and the resistome in the context of *Vibrio vulnificus* infection. By including both young and aged mice, it provided crucial insights into age-related vulnerabilities and advanced the understanding of how climate change-induced stressors impact gut and immune health. The study examined the effects of heat stress on aging, focusing on physiological, immunological, and microbial responses in a murine model. The research revealed that aging significantly increases vulnerability to environmental stressors, as shown by aged mice (24 months) exhibiting heightened sensitivity to periodic heat stress compared to younger mice (12 weeks). Key impacts included reduced food intake, compromised intestinal barrier integrity, and elevated inflammatory markers such as IL-1β. These changes collectively indicated diminished thermoregulatory capacity, increased systemic inflammation, and reduced resilience to heat stress. These findings underscore the elevated risks of morbidity and mortality faced by older adults, especially as climate change intensifies the frequency and severity of heatwaves. Aging naturally reduces thermoregulatory efficiency, with declines in sweat production, skin blood flow, and cardiovascular adaptability, which collectively increase the risk of heat-related illnesses such as heatstroke (Kenney et al., 2014). This vulnerability is compounded by immunosenescence, characterized by reductions in T-cell populations, chronic low-grade inflammation, and weakened immune responses. Heat stress exacerbates these age-related changes, further disrupting immune balance and amplifying inflammatory markers (Millyard et al., 2020), (Li et al., 2021). Heat stress was also found to impair intestinal barrier function and disrupt gut microbiota composition, leading to dysbiosis and systemic endotoxemia. These disruptions increase susceptibility to both enteric and systemic infections (Li et al., 2021). While climate change involves a range of environmental stressors, this study specifically focused on the thermal component. The repeated heat exposure model was designed to simulate the intensity and recurrence of heat waves that are projected to become more frequent. This allowed us to isolate and study the direct physiological and immunological impacts of sustained heat stress, particularly in the context of aging.

In this study, aged mice infected with *Vibrio vulnificus* after heat stress exhibited significantly higher levels of pro-inflammatory cytokines such as IL-1β, TNF-α, and IL-6, along with severe intestinal barrier damage and endotoxemia. The synergistic effects of heat stress and infection were most pronounced in aged mice compared to younger counterparts. Serum CRP levels and systemic inflammation markers were markedly elevated in the heat stress-plus-infection group compared to the infection-only group. Virulence factors of *Vibrio vulnificus*, such as the elastolytic protease VvpE, RtxA, hemolysin (VvhA), and peroxiredoxin (AhpCl), significantly induced pro-inflammatory cytokines (Shin et al., 2002), (Qin et al., 2019), (Huang et al., 2020), (Chuang et al., 2010), (Lee et al., 2018a), (Lee et al., 2018b). Cytokine dysregulation, particularly in the heat-stressed-plus-infection group, played a critical role in endotoxemia shock and high mortality. Elevated serum CRP levels and pronounced endotoxemia in this group further suggest that heat stress exacerbates the severity of *Vibrio vulnificus* infection. Immune dysfunction was another notable finding. Aged mice showed reduced CD4+ T-cell populations, increased immunosenescent CD4 + CD28− cells, and heightened cytotoxic CD8+ T-cell activity (Porciello et al., 2018), (Garrido-Rodríguez et al., 2021), (Ron et al., 2024). The decline in CD4+ T-cells and altered CD4/CD8 ratios were linked to inflammatory immunosenescent events. Heat stress further accelerated these changes, as indicated by increased intestinal

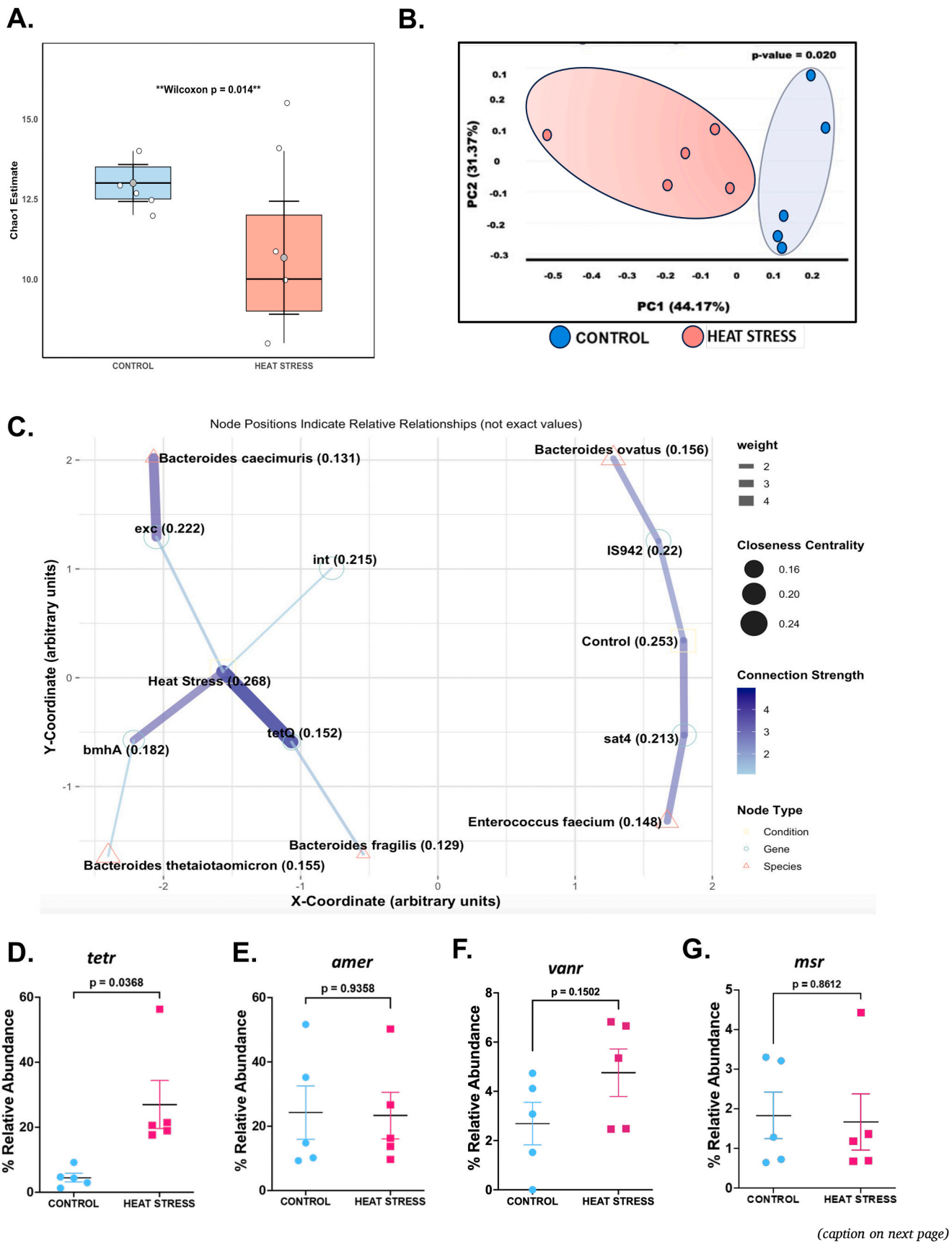

(caption on next page)

Fig. 7. Heat stress modified the composition of host gut-resistome and augmented resistance to clinically relevant antibiotics in aged mice. A. Diversity of resistome profile analysis showed as box plots depicting α-diversity (Chao1 index) in fecal samples from control and heat stress groups in aged mice ($n = 5$ biological replicates per group). Statistical significance was assessed using the Wilcoxon rank-sum test, with Benjamini-Hochberg correction applied for multiple comparisons ($p < 0.05$). Data are displayed as scatter plots with individual points representing biological replicates, overlaid with mean ± standard deviation (SD). B. Principal Coordinate Analysis (PCoA) representing antibiotic resistance genes (ARG) β-diversity (Bray-Curtis dissimilarity) in fecal samples from control and heat stress groups in aged mice ($n = 5$ biological replicates per group). The plot displays PC1 and PC2, which account for 44.17 % and 31.37 % of the total variance, respectively, showing distinct clustering of ARGs. Statistical analysis was performed using permutational multivariate analysis of variance (PERMANOVA), with significance determined at a threshold of $p < 0.05$. C. The network diagram representing relationships between virulence genes, bacterial species, and experimental conditions. Nodes are sized based on closeness centrality, reflecting their connectivity within the network, while edges represent interaction strengths, indicated by width and color gradient (light blue to dark blue). Associations such as *tetQ* with *Bacteroides fragilis* and heat stress conditions are highlighted, showcasing potential roles in adaptive resistance. The Fruchterman-Reingold layout optimally positions nodes for clear visualization. Axis labels provide coordinate reference in arbitrary units, enhancing spatial interpretation. Edge thickness and color intensity correspond to interaction strength. This network provided insights into microbial dynamics and the dissemination of resistance genes in response to environmental stress. D-F. Individual resistance gene abundance profiles for key antibiotic classes, including tetracycline resistance (tetr) (D), aminoglycoside resistance (amer) (E), vancomycin resistance (vanr) (F), and macrolide resistance (msr), (G) were presented as scatter plots with individual data points (n = 5 biological replicates). Statistical comparisons were conducted using the Wilcoxon rank-sum test, with significance set at $p < 0.05$. Statistical analysis was conducted using an unpaired, two-tailed *t*-test with Benjamini-Hochberg correction ($p < 0.05$). Bars indicate group means, with error bars representing standard deviation (SD).

cytotoxicity and systemic immune dysregulation. Serum cytokines (IL-1β, IL-6), intestinal IL-2, and serum IgA levels further confirmed enhanced immunosenescence in heat-stressed groups. These findings highlighted the age-dependent exacerbation of the pathophysiological impact of heat stress during *Vibrio vulnificus* infection and were further validated using an antibiotic-mediated gut depletion model.

Metagenomic sequencing revealed significant alterations in gut microbiota. Beneficial bacteria such as *Akkermansia muciniphila*, Mouse Japan SFB etc. known for their roles in gut barrier integrity and immune modulation, were reduced under heat stress (Fonseca et al., 2017), (Everard et al., 2013). Conversely, opportunistic pathogens like *Enterococcus faecalis*, *Clostridioides difficile* were enriched, contributing to dysbiosis and systemic inflammation. Adaptive increases in *Bifidobacterium pseudolongum*, *Lactobacillus johnsonii*, and *Roseburia intestinalis* were observed, with these species playing roles in maintaining immune balance and gut health. However, the effects of shifts in microbiota composition were more pronounced in aged mice, highlighting their increased vulnerability to heat stress-induced gut dysbiosis (Wen et al., 2021b), (Xia et al., 2022), (He et al., 2021), (Hylander and Repasky, 2019), (Huus and Ley, 2021).

Importantly this research validated the role of candidate microbial species induced by heat stress in a heat exposed model of antibiotic mediated gut depletion and supplementation recolonization. Probiotic interventions performed in gut depleted mice with *Roseburia intestinalis*, *Bifidobacterium pseudolongum* and *Akkermansia muciniphila* in presence or absence of periodic heat stress demonstrated potential in mitigating T-cell aging effects, improving intestinal barrier function although their efficacy varied, highlighting the need for tailored therapeutic strategies. This complex model was a unique approach developed to study the effects of heat stress related microbiome alterations in gut-immune axis.

In aged mice, sustained heat stress induced marked T cell dysregulation through a cascade of epithelial injury, microbial dysbiosis, and cytokine imbalance. Thermal exposure increased epithelial Hsp70 expression and systemic inflammation, reflected by elevated IL-6, TNF-α, and IL-1β, alongside a reduction in IL-2, a cytokine critical for T cell survival and proliferation. These immune shifts coincided with the depletion of microbial species essential for mucosal barrier maintenance and immune tolerance. The resulting dysbiosis and increased gut permeability likely triggered chronic immune activation and skewed T cell populations toward a senescent phenotype, evidenced by an increase in $CD4^{+}CD28^{-}$ cells and $CD8^{+}$ cytotoxic T cells. This immunological imbalance, coupled with expansion of pathobionts carrying virulence genes, compromised mucosal immunity and increased susceptibility to *Vibrio vulnificus* infection. Recolonization with *Roseburia intestinalis* reversed these effects by restoring IL-2 levels, reducing systemic inflammation, and rebalancing T cell subsets, while also improving epithelial integrity. These findings demonstrate the potential of targeted microbiota restoration to mitigate heat stress–induced immunosenescence and enhance host resistance to infection.

The enrichment of antibiotic resistance genes (ARGs), particularly those associated with tetracycline resistance, within the gut microbiota of aged mice raises additional concerns. The CDC recommends tetracycline as a treatment for *Vibrio vulnificus* infections (Liu et al., 2006), and heat stress-induced resistance may compromise treatment outcomes for elderly individuals exposed to periodic heatwaves. Probiotic interventions, such as *Roseburia intestinalis* and *Bifidobacterium pseudolongum*, demonstrated potential in mitigating dysbiosis and immune dysfunction, though their efficacy varied, underscoring the need for tailored therapeutic strategies.

Despite its significant contributions, this study has certain limitations. The absence of microbiome validation using a germ-free mouse model was due to infrastructural constraints, and the resistome analysis did not comprehensively identify the mechanism how ARGs are capable of transferring resistance to *Vibrio vulnificus*. Future research will address these gaps, including validating ARG findings in clinical strains.

5. Conclusions

This study established that climate change-induced heat stress acted in a compounded manner to exacerbate susceptibility to *Vibrio vulnificus* infection through disruption of the gut microbiome and immune axis. Aged mice subjected to periodic heat stress exhibited significantly compromised intestinal barrier function, elevated systemic inflammation, and enhanced immunosenescence compared to younger counterparts. Metagenomic analyses revealed substantial alterations in the gut microbiota, characterized by a depletion of beneficial species and an enrichment of opportunistic pathogens, alongside a notable increase in antibiotic resistance gene abundance, particularly tetracycline resistance. Functional experiments further demonstrated the involvement of gut microbiota in aggravated immune dysfunction under periodic heat stress, whereas recolonization with *Roseburia intestinalis*, *Bifidobacterium pseudolongum* and *Akkermansia muciniphila* partially restored gut integrity and mitigated T-cell aging under heat stress conditions. These findings underscored that periodic heat stress intensified age-related immune vulnerabilities, thereby amplifying infectious disease severity. Importantly, the data indicated that targeted modulation of the gut microbiome could serve as a potential intervention to counteract the deleterious impacts of climate-driven stressors on vulnerable populations. This work provided the first experimental evidence linking environmental heat stress-induced gut dysbiosis and immunological decline to heightened *Vibrio vulnificus* infection risk in aged hosts. Aging and heat stress together disrupted host microbiome and immune function, emphasizing the need for targeted interventions. Human studies in climate-sensitive regions are important to guide public health responses to increasing vibriosis risk. Given the accelerating pace of climate change and demographic shifts toward aging populations, these results

highlighted an urgent need for microbiota-centered therapeutic strategies to safeguard health outcomes against emerging environmental and pathogenic threats.

CRediT authorship contribution statement

Subhajit Roy: Writing – review & editing, Writing – original draft, Validation, Software, Methodology, Investigation, Formal analysis, Data curation. **Madhura More:** Writing – review & editing, Software, Methodology, Data curation. **Ayushi Trivedi:** Writing – review & editing, Methodology, Data curation. **Punnag Saha:** Methodology. **Dipro Bose:** Methodology. **Susmita Das:** Writing – review & editing. **Zahid Hayat Mahmud:** Writing – review & editing. **S.M. Manzoor Ahmed Hanifi:** Writing – review & editing. **Saurabh Chatterjee:** Writing – review & editing, Writing – original draft, Visualization, Validation, Supervision, Software, Resources, Project administration, Investigation, Funding acquisition, Formal analysis, Data curation, Conceptualization.

Declaration of Generative AI and AI-assisted technologies in the writing process

During the preparation of this work the author(s) used GPT 4o to improve language and readability. After using this tool, the author(s) reviewed and edited the content as needed and take(s) full responsibility for the content of the publication.

Funding statement

This study was supported by NIH/NIEHS Grant 1P01ES028942-01#Project 4 Toxicology awarded to Dr. Saurabh Chatterjee.

Declaration of competing interest

The authors declare that there is no conflict of financial or competing interests.

Acknowledgment

The authors gratefully acknowledge the technical services of AML Labs (St. Augustine, FL, USA), Experimental Tissue Resource (University of California, Irvine) for tissue processing and CosmosID Inc. (Germantown, MD, USA) for microbiome sequencing.

Appendix A. Supplementary data

Supplementary data to this article can be found online at https://doi.org/10.1016/j.scitotenv.2025.179881.

Data availability

Access to the entire sequencing data is available via the Sequence Read Archive (SRA) database, accession ID: PRJNA1106799, accessible at https://www.ncbi.nlm.nih.gov/sra/PRJNA1106799.

References

Ali, M.A., Kravitz, A.V., 2018. Challenges in quantifying food intake in rodents. Brain Res. 1693 (Pt B), 188–191. https://doi.org/10.1016/j.brainres.2018.04.007.

Amato, E., Riess, M., Thomas-Lopez, D., Linkevicius, M., Pitkänen, T., Wołkowicz, T., et al., 2022. Epidemiological and microbiological investigation of a large increase in vibriosis, northern Europe, 2018. Euro Surveill. 27 (28), 2200202. https://doi.org/10.2807/1560-7917.ES.2022.27.28.2200202.

Archer, E.J., Baker-Austin, C., Osborn, T.J., Jones, N.R., Martínez-Urtaza, J., Trinanes, J., et al., 2023. Climate warming and increasing *Vibrio vulnificus* infections in North America. Sci. Rep. 13 (1), 3893. https://doi.org/10.1038/s41598-023-30683-7.

Ballester, J., Quijal-Zamorano, M., Méndez Turrubiates, R.F., Pegenaute, F., Herrmann, F.R., Robine, J.M., et al., 2023. Heat-related mortality in Europe during the summer of 2022. Nat. Med. 29 (7), 1857–1866. https://doi.org/10.1038/s41591-023-02419-5.

Bastin, A., Karkey, L., Simpson, M., 2024. Climate change and cholera: a review exploring the association between storm severity and global human Vibrio spp. incidence. Georgetown Med. Rev. 8 (1) (No DOI available).

Bose, D., Chatterjee, S., Older, E., Seth, R., Janulewicz, P., Saha, P., et al., 2022. Host gut resistome in Gulf War chronic multisymptom illness correlates with persistent inflammation. Commun. Biol. 5 (1), 552. https://doi.org/10.1038/s42003-022-03512-4.

Bose, D., Saha, P., Roy, S., Trivedi, A., More, M., Klimas, N., et al., 2024. A double-humanized mouse model for studying host gut microbiome-immune interactions in Gulf War illness. Int. J. Mol. Sci. 25 (11), 5778. https://doi.org/10.3390/ijms25115778.

Centanni, M., Lawley, B., Butts, C.A., Roy, N.C., Lee, J., Kelly, W.J., et al., 2018. *Bifidobacterium pseudolongum* in the ceca of rats fed hi-maize starch has characteristics of a keystone species in bifidobacterial blooms. Appl. Environ. Microbiol. 84 (15), e00560-18. https://doi.org/10.1128/aem.00560-18.

Centers for Disease Control and Prevention (CDC), 2019. Annual Summary of Vibrio Illnesses Reported to the CDC. CDC, Atlanta, 2019. No DOI available.

Chuang, C.C., Chuang, Y.C., Chang, W.T., Chen, C.C., Hor, L.I., Huang, A.M., et al., 2010. Macrophage migration inhibitory factor regulates interleukin-6 production by facilitating nuclear factor-kappa B activation during Vibrio vulnificus infection. BMC Immunol. 11, 50. https://doi.org/10.1186/1471-2172-11-50.

Daharsh, L., Zhang, J., Ramer-Tait, A., Li, Q., 2019. A double humanized BLT-mice model featuring a stable human-like gut microbiome and human immune system. J. Vis. Exp. 150, e60029. https://doi.org/10.3791/60029.

Das, R., Nasrin, S., Palit, P., Sobi, R.A., Sultana, A.A., Khan, S.H., et al., 2023. *Vibrio cholerae* in rural and urban Bangladesh, findings from hospital-based surveillance, 2000–2021. Sci. Rep. 13 (1), 6411. https://doi.org/10.1038/s41598-023-33191-0.

DeBruyn, J.M., Hauther, K.A., 2017. Postmortem succession of gut microbial communities in deceased human subjects. PeerJ 5, e3437. https://doi.org/10.7717/peerj.3437.

Dingemanse, C., Belzer, C., van Hijum, S.A., Günthel, M., Salvatori, D., den Dunnen, J.T., et al., 2015. *Akkermansia muciniphila* and *Helicobacter typhlonius* modulate intestinal tumor development in mice. Carcinogenesis 36 (11), 1388–1395. https://doi.org/10.1093/carcin/bgv129.

Ebi, K.L., Capon, A., Berry, P., Broderick, C., de Dear, R., Havenith, G., et al., 2021a. Hot weather and heat extremes: health risks. Lancet 398 (10301), 698–708. https://doi.org/10.1016/S0140-6736(21)01208-3.

Ebi, K.L., Vanos, J., Baldwin, J.W., Bell, J.E., Hondula, D.M., Errett, N.A., et al., 2021b. Extreme weather and climate change: population health and health system implications. Annu. Rev. Public Health 42, 293–315. https://doi.org/10.1146/annurev-publhealth-012420-105026.

Ericsson, A.C., Franklin, C.L., 2021. The gut microbiome of laboratory mice: considerations and best practices for translational research. Mamm. Genome 32 (4), 239–250. https://doi.org/10.1007/s00335-021-09868-7.

Everard, A., Belzer, C., Geurts, L., Ouwerkerk, J.P., Druart, C., Bindels, L.B., et al., 2013. Cross-talk between Akkermansia muciniphila and intestinal epithelium controls diet-induced obesity. Proc. Natl. Acad. Sci. U. S. A. 110 (22), 9066–9071. https://doi.org/10.1073/pnas.1219451110.

Festing, M.F., Altman, D.G., 2002. Guidelines for the design and statistical analysis of experiments using laboratory animals. ILAR J. 43 (4), 244–258. https://doi.org/10.1093/ilar.43.4.244.

Fleischmann, S., Herrig, I., Wesp, J., Stiedl, J., Reifferscheid, G., Strauch, E., et al., 2022. Prevalence and distribution of potentially human pathogenic Vibrio spp. on German North and Baltic Sea coasts. Front. Cell. Infect. Microbiol. 12, 846819. https://doi.org/10.3389/fcimb.2022.846819.

Fonseca, W., Lucey, K., Jang, S., Fujimura, K.E., Rasky, A., Ting, H.A., et al., 2017. *Lactobacillus johnsonii* supplementation attenuates respiratory viral infection via metabolic reprogramming and immune cell modulation. Mucosal Immunol. 10 (6), 1569–1580. https://doi.org/10.1038/mi.2017.15.

Garrido-Rodríguez, V., Herrero-Fernández, I., Castro, M.J., Castillo, A., Rosado-Sánchez, I., Galvá, M.I., et al., 2021. Immunological features beyond CD4/CD8 ratio values in older individuals. Aging (Albany NY) 13 (10), 13443–13459. https://doi.org/10.18632/aging.203016.

Gavin, H.E., Satchell, K.J.F., 2017. Surface hypothermia predicts murine mortality in the intragastric *Vibrio vulnificus* infection model. BMC Microbiol. 17 (1), 136. https://doi.org/10.1186/s12866-017-1048-5.

Grundstein, A., Dowd, J., 2011. Trends in extreme apparent temperatures over the United States, 1949–2010. J. Appl. Meteorol. Climatol. 50 (8), 1650–1653. https://doi.org/10.1175/2011JAMC2627.1.

Hammami, M.M., Bouchama, A., Shail, E., Aboul-Enein, H.Y., Al-Sedairy, S., 1998. Lymphocyte subsets and adhesion molecules expression in heatstroke and heat stress. J. Appl. Physiol. 84 (5), 1615–1621. https://doi.org/10.1152/jappl.1998.84.5.1615.

Hänninen, A., Toivonen, R., Pöysti, S., Belzer, C., Plovier, H., Ouwerkerk, J.P., et al., 2018. Akkermansia muciniphila induces gut microbiota remodelling and controls islet autoimmunity in NOD mice. Gut 67 (8), 1445–1453. https://doi.org/10.1136/gutjnl-2017-314508.

Hassan, F.U., Nawaz, A., Rehman, M.S., Ali, M.A., Dilshad, S.M.R., Yang, C., 2019. Prospects of HSP70 as a genetic marker for thermo-tolerance and immuno-modulation in animals under climate change scenario. Anim. Nutr. 5 (4), 340–350. https://doi.org/10.1016/j.aninu.2019.08.004.

Hayhoe, K., Cayan, D., Field, C.B., Frumhoff, P.C., Maurer, E.P., Miller, N.L., et al., 2004. Emissions pathways, climate change, and impacts on California. Proc. Natl. Acad. Sci. U. S. A. 101 (34), 12422–12427. https://doi.org/10.1073/pnas.0404500101.

He, Y., Maltecca, C., Tiezzi, F., 2021. Potential use of gut microbiota composition as a biomarker of heat stress in monogastric species: a review. Animals (Basel) 11 (6), 1637. https://doi.org/10.3390/ani11061637.

Hegde, S.T., Khan, A.I., Perez-Saez, J., Khan, I.I., Hulse, J.D., Islam, M.T., et al., 2024. Clinical surveillance systems obscure the true cholera infection burden in an endemic region. Nat. Med. 30 (3), 888–895. https://doi.org/10.1038/s41591-024-02719-4.

Hirakawa, R., Nurjanah, S., Furukawa, K., Murai, A., Kikusato, M., Nochi, T., et al., 2020. Heat stress causes immune abnormalities via massive damage to lymphocyte proliferation and differentiation in broiler chickens. Front Vet Sci. 7, 46. https://doi.org/10.3389/fvets.2020.00046.

Horseman, M.A., Surani, S., 2011. A comprehensive review of Vibrio vulnificus: an important cause of severe sepsis and skin and soft-tissue infection. Int. J. Infect. Dis. 15 (3), e157–e166. https://doi.org/10.1016/j.ijid.2010.11.003.

Hu, C., Patil, Y., Gong, D., Yu, T., Li, J., Wu, L., et al., 2022. Heat stress-induced dysbiosis of porcine colon microbiota plays a role in intestinal damage: a fecal microbiota profile. Front Vet Sci. 9, 686902. https://doi.org/10.3389/fvets.2022.686902.

Huang, X.H., Ma, Y., Lou, H., Chen, N., Zhang, T., Wu, L.Y., et al., 2020. The role of TSC1 in the macrophages against Vibrio vulnificus infection. Front. Cell. Infect. Microbiol. 10, 596609. https://doi.org/10.3389/fcimb.2020.596609.

Hughes, M.J., Flaherty, E., Lee, N., Robbins, A., Weller, D.L., 2024. Notes from the field: severe Vibrio vulnificus infections during heat waves - three Eastern U.S. states, July–August 2023. MMWR Morb. Mortal. Wkly Rep. 73 (4), 84–85. https://doi.org/10.15585/mmwr.mm7304a3.

Huus, K.E., Ley, R.E., 2021. Blowing hot and cold: body temperature and the microbiome. mSystems 6 (5), e0070721. https://doi.org/10.1128/mSystems.00707-21.

Hylander, B.L., Repasky, E.A., 2019. Temperature as a modulator of the gut microbiome: what are the implications and opportunities for thermal medicine? Int. J. Hyperthermia. 36 (sup1), 83–89. https://doi.org/10.1080/02656736.2019.1650173.

Islam, M.T., Hegde, S.T., Khan, A.I., Bhuiyan, M.T.R., Khan, Z.H., Ahmmed, F., et al., 2023. National hospital-based sentinel surveillance for cholera in Bangladesh: epidemiological results from 2014 to 2021. Am. J. Trop. Med. Hyg. 109 (3), 575–583. https://doi.org/10.4269/ajtmh.22-0702.

Kamada, N., Seo, S.U., Chen, G.Y., Núñez, G., 2013. Role of the gut microbiota in immunity and inflammatory disease. Nat. Rev. Immunol. 13 (5), 321–335. https://doi.org/10.1038/nri3430.

Kang, X., Liu, C., Ding, Y., Ni, Y., Ji, F., Lau, H.C.H., et al., 2023. *Roseburia intestinalis*-generated butyrate boosts anti-PD-1 efficacy in colorectal cancer by activating cytotoxic CD8(+) T cells. Gut 72 (11), 2112–2122. https://doi.org/10.1136/gutjnl-2022-328288.

Kenney, W.L., Craighead, D.H., Alexander, L.M., 2014. Heat waves, aging, and human cardiovascular health. Med. Sci. Sports Exerc. 46 (10), 1891–1899. https://doi.org/10.1249/MSS.0000000000000325.

Knowlton, K., Lynn, B., Goldberg, R.A., Rosenzweig, C., Hogrefe, C., Rosenthal, J.K., et al., 2007. Projecting heat-related mortality impacts under a changing climate in the New York City region. Am. J. Public Health 97 (11), 2028–2034. https://doi.org/10.2105/AJPH.2006.102947.

Koch, F., Thom, U., Albrecht, E., Weikard, R., Nolte, W., Kuhla, B., et al., 2019. Heat stress directly impairs gut integrity and recruits distinct immune cell populations into the bovine intestine. Proc. Natl. Acad. Sci. U. S. A. 116 (21), 10333–10338. https://doi.org/10.1073/pnas.1818958116.

Kundra, P., Geirnaert, A., Pugin, B., Plüss, S., Kariluoto, S., Lacroix, C., et al., 2024. Microbially-produced folate forms support the growth of *Roseburia intestinalis* but not its competitive fitness in fecal batch fermentations. BMC Microbiol. 24 (1), 366. https://doi.org/10.1186/s12866-024-03273-5.

Lee, W., Moon, M., Kim, H.G., Lee, T.H., Oh, M.S., 2015. Heat stress-induced memory impairment is associated with neuroinflammation in mice. J. Neuroinflammation 12, 102. https://doi.org/10.1186/s12974-015-0314-0.

Lee, A., Kim, M.S., Cho, D., Jang, K.K., Choi, S.H., Kim, T.S., 2018a. Vibrio vulnificus RtxA is a major factor driving inflammatory T helper type 17 cell responses in vitro and in vivo. Front. Immunol. 9, 2095. https://doi.org/10.3389/fimmu.2018.02095.

Lee, A., Lim, H.X., Kim, M.S., Cho, D., Jang, K.K., Choi, S.H., et al., 2018b. *Vibrio vulnificus* infection induces the maturation and activation of dendritic cells with inflammatory Th17-polarizing ability. Int. J. Mol. Med. 41 (1), 531–540. https://doi.org/10.3892/ijmm.2017.3248.

Li, Y., Xie, X., Shi, X., Lin, Y., Qiu, Y., Mou, J., et al., 2014. Vibrio parahaemolyticus, southern coastal region of China, 2007–2012. Emerg. Infect. Dis. 20 (4), 685–688. https://doi.org/10.3201/eid2004.130744.

Li, W.H., Liu, Y.L., Lun, J.C., He, Y.M., Tang, L.P., 2021. Heat stress inhibits TLR4-NF-κB and TLR4-TBK1 signaling pathways in broilers infected with *Salmonella typhimurium*. Int. J. Biometeorol. 65 (11), 1895–1903. https://doi.org/10.1007/s00484-021-02166-w.

Lipinski, J.H., Zhou, X., Gurczynski, S.J., Erb-Downward, J.R., Dickson, R.P., Huffnagle, G.B., et al., 2021. Cage environment regulates gut microbiota independent of toll-like receptors. Infect. Immun. 89 (9), e0018721. https://doi.org/10.1128/iai.00187-21.

Liu, J.W., Lee, I.K., Tang, H.J., Ko, W.C., Lee, H.C., Liu, Y.C., et al., 2006. Prognostic factors and antibiotics in Vibrio vulnificus septicemia. Arch. Intern. Med. 166 (19), 2117–2123. https://doi.org/10.1001/archinte.166.19.2117.

Logar-Henderson, C., Ling, R., Tuite, A.R., Fisman, D.N., 2019. Effects of large-scale oceanic phenomena on non-cholera vibriosis incidence in the United States: implications for climate change. Epidemiol. Infect. 147, e243. https://doi.org/10.1017/S095026881900130X.

Luo, M., Wu, S., Lau, G.N., Pei, T., Liu, Z., Wang, X., et al., 2024. Anthropogenic forcing has increased the risk of longer-traveling and slower-moving large contiguous heatwaves. Sci. Adv. 10 (13), eadl1598. https://doi.org/10.1126/sciadv.adl1598.

Marx, W., Haunschild, R., Bornmann, L., 2021. Heat waves: a hot topic in climate change research. Theor. Appl. Climatol. 146 (1–2), 781–800. https://doi.org/10.1007/s00704-021-03705-4.

McMichael, A.J., Lindgren, E., 2011. Climate change: present and future risks to health, and necessary responses. J. Intern. Med. 270 (5), 401–413. https://doi.org/10.1111/j.1365-2796.2011.02415.x.

Millyard, A., Layden, J.D., Pyne, D.B., Edwards, A.M., Bloxham, S.R., 2020. Impairments to thermoregulation in the elderly during heat exposure events. Gerontol Geriatr Med. 6, 2333721420932432. https://doi.org/10.1177/2333721420932432.

Quickstats: percentage distribution of heat-related deaths, by age group - National Vital Statistics System, United States, 2018–2020. MMWR Morb. Mortal. Wkly. Rep. 71 (24), 2022, 808. https://doi.org/10.15585/mmwr.mm7124a4.

Morgado, M.E., Brumfield, K.D., Chattopadhyay, S., Malayil, L., Alawode, T., Amokeodo, I., et al., 2024. Antibiotic resistance trends among Vibrio vulnificus and Vibrio parahaemolyticus isolated from the Chesapeake Bay, Maryland: a longitudinal study. Appl. Environ. Microbiol. 90 (6), e0053924. https://doi.org/10.1128/aem.00539-24.

Paone, P., Cani, P.D., 2020. Mucus barrier, mucins and gut microbiota: the expected slimy partners? Gut 69 (12), 2232–2243. https://doi.org/10.1136/gutjnl-2020-321018.

Parvin, I., Shahid, A., Das, S., Shahrin, L., Ackhter, M.M., Alam, T., et al., 2021. *Vibrio cholerae* O139 persists in Dhaka, Bangladesh since 1993. PLoS Negl. Trop. Dis. 15 (9), e0009721. https://doi.org/10.1371/journal.pntd.0009721.

Perkins-Kirkpatrick, S.E., Lewis, S.C., 2020. Increasing trends in regional heatwaves. Nat. Commun. 11 (1), 3357. https://doi.org/10.1038/s41467-020-16970-7.

Porciello, N., Grazioli, P., Campese, A.F., Kunkl, M., Caristi, S., Mastrogiovanni, M., et al., 2018. A non-conserved amino acid variant regulates differential signalling between human and mouse CD28. Nat. Commun. 9 (1), 1080. https://doi.org/10.1038/s41467-018-03432-8.

Qin, K., Fu, K., Liu, J., Wu, C., Wang, Y., Zhou, L., 2019. Vibrio vulnificus cytolysin induces inflammatory responses in RAW264.7 macrophages through calcium signaling and causes inflammation in vivo. Microb. Pathog. 137, 103789. https://doi.org/10.1016/j.micpath.2019.103789.

Qu, Q., Li, H., Bai, L., Zhang, S., Sun, J., Lv, W., et al., 2021. Effects of heat stress on gut microbiome in rats. Indian J. Microbiol. 61 (3), 338–347. https://doi.org/10.1007/s12088-021-00948-4.

Riedinger, D.J., Fernández, J.V., Delgado, L.F., et al., 2024. Control of *Vibrio vulnificus* proliferation in the Baltic Sea through eutrophication and algal bloom management. Commun. Earth Environ. 5, 246. https://doi.org/10.1038/s43247-024-01211-2.

Ron, R., Martínez-Sanz, J., Herrera, S., Ramos-Ruperto, L., Díez, A., Sainz, T., et al., 2024. CD4/CD8 ratio and CD8+ T-cell count as prognostic markers for non-AIDS mortality in people living with HIV: a systematic review and meta-analysis. Front. Immunol. 15, 1343124. https://doi.org/10.3389/fimmu.2024.1343124.

Roy, S., Saha, P., Bose, D., Chatterjee, S., 2023. Host gut-resistome and gut-immune axes are the key to non-cholera Vibrio infection severity in aging and heat stress. J. Immunol. 210 (1 Suppl), 81.02. https://doi.org/10.4049/jimmunol.210.Supp.81.02.

Roy, S., Saha, P., Bose, D., Trivedi, A., More, M., Lin, C., et al., 2024. Periodic heat waves-induced neuronal etiology in the elderly is mediated by gut-liver-brain axis: a transcriptome profiling approach. Sci. Rep. 14 (1), 10555. https://doi.org/10.1038/s41598-024-47852-9.

Saha, P., Bose, D., Stebliankin, V., Cickovski, T., Seth, R.K., Porter, D.E., et al., 2022. Prior exposure to microcystin alters host gut resistome and is associated with dysregulated immune homeostasis in translatable mouse models. Sci. Rep. 12 (1), 11516. https://doi.org/10.1038/s41598-022-15631-7.

Sharma, H.S., Kretzschmar, R., Cervós-Navarro, J., Ermisch, A., Rühle, H.J., Dey, P.K., 1992. Age-related pathophysiology of the blood-brain barrier in heat stress. Prog. Brain Res. 91, 189–196. https://doi.org/10.1016/s0079-6123(08)62406-4.

Sheahan, M., Gould, C.A., Neumann, J.E., Kinney, P.L., Hoffmann, S., Fant, C., et al., 2022. Examining the relationship between climate change and vibriosis in the United States: projected health and economic impacts for the 21st century. Environ. Health Perspect. 130 (8), 087007. https://doi.org/10.1289/EHP10838.

Shen, Z., Luo, W., Tan, B., Nie, K., Deng, M., Wu, S., et al., 2022. Roseburia intestinalis stimulates TLR5-dependent intestinal immunity against Crohn's disease. EBioMedicine 85, 104285. https://doi.org/10.1016/j.ebiom.2022.104285.

Shin, S.H., Shin, D.H., Ryu, P.Y., Chung, S.S., Rhee, J.H., 2002. Proinflammatory cytokine profile in *Vibrio vulnificus* septicemic patients' sera. FEMS Immunol. Med. Microbiol. 33 (2), 133–138. https://doi.org/10.1016/s0928-8244(01)00260-8.

Shishir, M.A., Mamun, M.A., Mian, M.M., Ferdous, U.T., Akter, N.J., Suravi, R.S., et al., 2018. Prevalence of Vibrio cholerae in coastal alternative supplies of drinking water and association with Bacillus-like spore formers. Front. Public Health 6, 50. https://doi.org/10.3389/fpubh.2018.00050.

Siddiqui, S.H., Kang, D., Park, J., Khan, M., Shim, K., 2020. Chronic heat stress regulates the relation between heat shock protein and immunity in broiler small intestine. Sci. Rep. 10 (1), 18872. https://doi.org/10.1038/s41598-020-75756-1.

Song, Q., Zhang, X., Liu, W., Wei, H., Liang, W., Zhou, Y., et al., 2023. *Bifidobacterium pseudolongum*-generated acetate suppresses non-alcoholic fatty liver disease-associated hepatocellular carcinoma. J. Hepatol. 79 (6), 1352–1365. https://doi.org/10.1016/j.jhep.2023.07.016.

Starks, A.M., Schoeb, T.R., Tamplin, M.L., Parveen, S., Doyle, T.J., Bomeisl, P.E., et al., 2000. Pathogenesis of infection by clinical and environmental strains of Vibrio vulnificus in iron-dextran-treated mice. Infect. Immun. 68 (10), 5785–5793. https://doi.org/10.1128/IAI.68.10.5785-5793.2000.

Tirelle, P., Breton, J., Riou, G., Déchelotte, P., Coëffier, M., Ribet, D., 2020. Comparison of different modes of antibiotic delivery on gut microbiota depletion efficiency and body composition in mouse. BMC Microbiol. 20 (1), 340. https://doi.org/10.1186/s12866-020-02024-6.

Trinanes, J., Martinez-Urtaza, J., 2021. Future scenarios of risk of Vibrio infections in a warming planet: a global mapping study. Lancet Planet Health 5 (7), e426–e435. https://doi.org/10.1016/S2542-5196(21)00130-4.

Victor, J.D., 1988. Evaluation of poor performance and asymmetry in the Farnsworth-Munsell 100-hue test. Invest. Ophthalmol. Vis. Sci. 29 (3), 476–481 (No DOI available).

Wen, C., Wei, S., Zong, X., Wang, Y., Jin, M., 2021a. Microbiota-gut-brain axis and nutritional strategy under heat stress. Anim Nutr. 7 (4), 1329–1336. https://doi.org/10.1016/j.aninu.2021.03.008.

Wen, C., Li, S., Wang, J., Zhu, Y., Zong, X., Wang, Y., et al., 2021b. Heat stress alters the intestinal microbiota and metabolomic profiles in mice. Front. Microbiol. 12, 706772. https://doi.org/10.3389/fmicb.2021.706772.

Witjes, V.M., Boleij, A., Halffman, W., 2020. Reducing versus embracing variation as strategies for reproducibility: the microbiome of laboratory mice. Animals (Basel). 10 (12), 2380. https://doi.org/10.3390/ani10122380.

Xia, B., Wu, W., Fang, W., Wen, X., Xie, J., Zhang, H., 2022. Heat stress-induced mucosal barrier dysfunction is potentially associated with gut microbiota dysbiosis in pigs. Anim Nutr. 8 (1), 289–299. https://doi.org/10.1016/j.aninu.2021.08.013.

Yang, C., Dong, J., Sun, C., Li, W., Tian, Y., Liu, Z., et al., 2022. Exposure to heat stress causes downregulation of immune response genes and weakens the disease resistance of Micropterus salmoides. Comp. Biochem. Physiol. Part D Genomics Proteomics 43, 101011. https://doi.org/10.1016/j.cbd.2022.101011.

Zaidenstein, R., Sadik, C., Lerner, L., Valinsky, L., Kopelowitz, J., Yishai, R., et al., 2008. Clinical characteristics and molecular subtyping of *Vibrio vulnificus* illnesses, Israel. Emerg. Infect. Dis. 14 (12), 1875–1882. https://doi.org/10.3201/eid1412.071541.

Zanobetti, A., O'Neill, M.S., Gronlund, C.J., Schwartz, J.D., 2012. Summer temperature variability and long-term survival among elderly people with chronic disease. Proc. Natl. Acad. Sci. U. S. A. 109 (17), 6608–6613. https://doi.org/10.1073/pnas.1113070109.

Zheng, D., Liwinski, T., Elinav, E., 2020. Interaction between microbiota and immunity in health and disease. Cell Res. 30 (6), 492–506. https://doi.org/10.1038/s41422-020-0332-7.